Understanding structure-activity relationships in highly active La promoted Ni catalysts for CO2 methanation

Understanding structure-activity relationships in highly active La promoted Ni catalysts for CO₂ methanation

Phuoc Hoang Ho[1], Giancosimo Sanghez de Luna[1], Saverio Angelucci[1,2], Andrea Canciani[1,2], Wilm Jones[2,3], Donato Decarolis[2], Francesca Ospitali[1], Elena Rodriguez Aguado[4], Enrique Rodríguez-Castellón[4], Giuseppe Fornasari[1], Angelo Vaccari[1], Andrew M. Beale[2,3]*, Patricia Benito[1,]*

[1] Dip. Chimica Industriale "Toso Montanari", Università di Bologna, Viale Risorgimento 4, 40136, Bologna, Italy

[2] Research Complex at Harwell, Rutherford Appleton Laboratories, Harwell, OX11 0FA, Oxon. UK

[3] Department of Chemistry, 20 Gordon Street, University College London, WC1H 0AJ, London. UK

[4] Departamento de Química Inorgánica, Facultad de Ciencias, Universidad de Málaga, 29071 Málaga, Spain

* patricia.benito3@unibo.it

* andrew.beale@ucl.ac.uk

ABSTRACT

Ni-based catalysts are selective in the hydrogenation of CO_2 to CH_4 but their activity and stability need improvement. Herein, we propose a hydrotalcite-derived high loaded $Ni-Al_2O_3$ catalyst promoted by La. The effect of La on the catalyst properties is investigated and compared with that of Y and Ce. The NiO_x crystallite size and basic properties (rather than the nickel reducibility) as well as the catalytic activity depend on the rare-earth element. The La-catalyst achieves a more relevant activity enhancement at low temperature and high space velocity (480 L g^{-1} h^{-1}, $CO_2/H_2/N_2$ = 1/4/1 v/v), high CH_4 productivity (101 L_{CH4} g_{Ni}^{-1} h^{-1}) and stability, even under undiluted feeds. *In situ* DRIFTS and the characterization of spent catalysts confirm that this enhanced performance is related to the combination of dissociative and associative CO_2 activation on more reduced, highly dispersed and stable Ni nanoparticles and basic sites in the $La_2O_3-Al_2O_3$ matrix, respectively.

Keywords: Nickel, Lanthanum, hydrotalcite, CO_2, methanation

1. Introduction

The hydrogenation of CO_2 to CH_4 (Sabatier reaction) constitutes one of the most promising Power to Gas (PtG) technologies for long-term and high capacity CO_2 utilization as well as renewable energy storage [1,2]. The gas produced in a highly active and selective CO_2 conversion can be fed into the existing gas grid after simple water separation. Thus, large efforts have been made in the last years to move from the laboratory to the pilot [3-8] and industrial scale [9,10]. The hydrogenation of CO_2 to CH_4 is highly exothermic (-165 kJ/mol), thermodynamically favored at low temperature and high pressure, though the kinetics increase with the temperature [11]. Hence, the success of this process depends on a combination of both catalyst activity and selectivity at low temperature in addition to heat management [12].

Ni-based catalysts are active and cheap and are therefore considered to be perhaps the best option for industrial application. Indeed, Ni/Al_2O_3 is currently employed as commercial methanation catalysts although they are mainly used to convert CO [13]. Methanation performance is widely related to Ni loading and reducibility [14], metal particle size [15], alloy formation (e.g. NiFe) [16] and support properties [17], which determine the activation of both H_2 and CO_2, as well as the stability and interaction among reaction intermediates to produce CH_4. However, recently it has been stated that CO_2 methanation is structure insensitive on the most active highly metal- loaded Ni/Al_2O_3 catalysts [18]. The turnover frequency (TOF) does not depend on metal-support interaction, metal-support interface or particle size, but on the total Ni surface area, which is highly dependent on the preparation method. Whereas, the basicity of the support controls the adsorption capability towards CO_2 and hence, the activation mechanism e.g. through CO or formate species [17]. Consistent with the 'Sabatier principle', medium basicity is widely accepted as optimal [19], though in some studies weak and strong basic sites are also reported as active [20, 21]. Clearly, the role of the support goes beyond simple CO_2 activation; it modifies the properties of Ni-containing species and, therefore, both H_2 and CO_2 activation.

Rare-earth elements, mainly, La, Ce, and Y, have been shown to increase the performance at low temperature, a behaviour related to a higher basicity, enhanced Ni reducibility and/or smaller Ni particles [22-32]. Moreover, the tolerance to sulfur increases for CeO_2-promoted catalysts [33]. Obviously, the catalyst properties (chemical-physical and performance) depend on the type and quantity of rare-earth elements. CO species are detected over Ni/Al_2O_3, only carbonates on Ni/La_2O_3, whereas formates are quickly decomposed on Ni/Y_2O_3 [17]. Alcalde-Santiago et al. [34] compared Ni/CeO_2 and Ni/La_2O_3 catalysts evidencing the role of the support on the modification of Ni-containing species and on the stability of surface H_2O and CO_2. Differences in the CO_2 methanation mechanism using Ni/CeO_2 and Ni/Al_2O_3 catalysts have been evidenced by isotopic and in situ DRIFTS [35]. Ni/CeO_2 provides different active sites for CO_2 and H_2 dissociation as well as for water desorption. In Ni/Al_2O_3 catalysts, rare-earth elements modify the interactions of Ni with the support and the type of reaction intermediates. For instance, CeO_2 on Ni/Al_2O_3 decrease the formation of $NiAl_2O_4$ [24]. Based on DRIFTS measurements, Gac et al. proposed that when CeO_2 is present as a promoter in Ni/Al_2O_3 it leads to enhancement in the formation of intermediate formates [30]. The basicity of the La_2O_3-Al_2O_3 support favors a stronger adsorption of carbonates that act as reactant reservoirs [31]. Despite some similarities between Ni on pure rare-earth oxides and on modified Al_2O_3 there is no straightforward correlation with catalytic performance. Strikingly, the trend in the activity is $Y_2O_3 > CeO_2 > Al_2O_3 > La_2O_3$ for Ni supported on pure oxides [17] yet when these oxides are used to modify Ni/Al_2O_3, the trend changes accordingly to $La_2O_3 > CeO_2 > Y_2O_3$ [27]. In contrast, Italiano et al. reported that for 15 wt.% Ni supported on pure oxides, the activity performance decreases in the order $Y_2O_3 > Al_2O_3 > CeO_2$ [36]; Ni/CeO_2 deactivated by coke deposition. The dispersion of Ni and rare-earth elements, the interaction between them and with the oxide matrix may be responsible for these apparently contradictory behaviors, though this has not specified in the literature. Moreover, the aforementioned features could be also related to the rare-earth loading (e.g. from 100 to 2 wt.%) as well as to the deposition/incorporation method of both of them on/into the Al_2O_3 support; to date incipient wetness impregnation [14], wet impregnation [27] (depositing Ni^{2+} and Ln^{3+},

4

simultaneously or in consecutive steps), one-pot sol gel [25] or coprecipitation [32] have been used to prepare such catalysts.

NiAl hydrotalcite-derived (HT) catalysts, prepared by coprecipitation and calcination, have been shown to be more active [37] and stable than commercial impregnated catalysts [38], since they are characterized by a high dispersion and stability of Ni^0 particles, even at high Ni loadings [39, 40]. However, under ageing conditions [38] or high CO_2 conversions prone to hot spots [41] coprecipitated catalysts deactivate. Ni particle sintering, loss of surface area, reduction of CO_2 adsorption capacity and medium basic sites, as well as structural changes occur [38]. Moreover, $Ni(OH)_2$ formation has been recently claimed, decreasing the active phase (Ni^0), and favoring the sintering and formation of inactive species (notably surface $NiAl_2O_4$) [42].

The use of rare-earth element promoted hydrotalcite precursors therefore holds much promise in realizing the next generation of Ni-based catalysts for CO_2 hydrogenation. For example, it has been shown that for NiMgAl HT-derived catalysts ($Ni_{68}Mg_{6.7}La_{1.5}Al_{23.5}$), the presence of additional La changes the interaction between Ni and periclase (chemical nature and oxidation state) and increases the number of medium and strong basic sites in a catalyst reduced at 900°C [32], the La effect depending on the preparation method [43] and the La loading [44, 45]. NiMgAl in comparison to NiAl shows smaller and more stabilized Ni^0 particles, however, these Ni species are hardly reducible, requiring very high temperatures (900 °C) [32, 46, 47], which subsequently modifies the crystalline phases and decreases the surface area in comparison to using a HT precursor calcined at moderate temperatures (ca. 450-600 °C) and alters the basic properties [48-50].

The aim of this work is to unravel the effect of La in a high loaded coprecipitated $Ni-La_2O_3-Al_2O_3$ catalyst, produced via calcination and reduction at 600 °C of a NiLaAl-HT material (Ni/La/Al = 70/5/25 atomic ratio) and compare its effect with those of Ce and Y, keeping constant the atomic ratio. The link between the chemical-physical properties (especially the metallic particle size and basic sites trade-off) and the activity and CO_2 activation mechanism of the promoted bulk catalysts,

which to date has been rarely reported, has been elucidated. This is followed by their testing for CO_2 methanation under harsh reaction conditions with $CO_2/H_2/N_2 = 1/4/1$ and $1/4/0$ (v/v) feedstock at high space velocity values, by measuring temperature profiles along the centerline of the bed and in turn analyzing the contribution of the heat generated during the exothermic process (barely considered in the literature). The reaction mechanism is elucidated using *in situ* DRIFTs whilst feeding a reaction mixture ($CO_2/H_2/N_2 = 1/4/1$ v/v) at low oven temperatures. The stability of the La catalyst is investigated under transient conditions (shut-down and start-up), important for the Power to Gas technology [51], but to the best of our knowledge, is scarcely reported [52, 53].

2. Experimental part

2.1. Catalyst synthesis

The catalysts were prepared by coprecipitation at constant pH 10.0. In a typical synthesis, 1.0 M nitrate solution of Ni/Al = 75/25 or Ni/X/Al = 70/5/25 (atomic ratio) (where X = La, Y, or Ce) was dropped ($\sim$ 2 mL min^{-1}) into a batch reactor containing 2.0 M Na_2CO_3 solution at 60 $^{\circ}$C under stirring by a magnetic bar at 750 rpm. The pH was controlled at 10.0 ± 0.1 by dropwise addition of a 3.0 M NaOH solution. The amount of Na_2CO_3 was calculated by charge balance of the HT system when a trivalent cation substituted a divalent one in the brucite structure with an excess amount of three-fold. After aging for 1 h at 60 $^{\circ}$C, the resulted slurry was filtered and washed thoroughly with distilled water until pH 7.0. The filtration cake was dried at 60 $^{\circ}$C for 24 h and then ground to obtain a fine powder of HT catalyst precursors. These precursors were subsequently calcined at 600 $^{\circ}$C (ramp 10 $^{\circ}$C min^{-1}) for 6 h in static oven. The catalysts were named as NiAl or NiXAl where X = La, Y, or Ce. The effect rare-earth elements, with loadings similar to those reported for impregnated catalysts [29, 31], on the properties of the catalysts has been investigated by keeping constant the atomic ratio composition. The role of the amount of rare-earth elements, albeit modifying the activity [29, 31, 44, 45], is out of scope of this work. For catalytic tests, the calcined powder catalysts were pelletized

using a Specac laboratory hydraulic press. The pellet was ground in a mortar and a fraction of materials with particle size in range of 0.420-0.595 mm (sieve mesh number 40 – 30) was collected.

2.2. Characterization techniques

X-ray diffraction (XRD) analysis was carried out using a PANalytical X'Pert diffractometer equipped with a Cu-K$_\alpha$ radiation (λ_{mean} = 0.15418 nm) and a fast X'Celerator detector. Wide-angle diffractogram was collected over 2θ range from 5 to 80° with a step size of 0.05° and scan time 15.25 s per step. The mean NiO and Ni^0 crystallite sizes, d_c, were determined using the Scherrer equation for NiO (200) and Ni^0 (002) planes, respectively. The shape factor, K$_F$, was 0.9.

Specific surface area of the catalyst was determined by N$_2$ adsorption/desorption at -196 °C using a Micromeritics ASAP 2020 instrument. Samples (0.15 g powder catalysts) were degassed under vacuum (< 30 µm Hg) at 150 °C for HT precursors (or at 250 °C for calcined catalysts) and maintained for 30 min before performing the measurement. The specific surface area (S$_{BET}$) was calculated using the Brunauer-Emmett-Teller (BET) multiple-point method in the relative pressure range p/p^0 from 0.05 to 0.3. Total pore volume V$_{Pore}$ was calculated at p/p^o = 0.99 from adsorption data branch.

Hydrogen temperature programmed reduction (H$_2$-TPR) was performed in an AutoChem II (Chemisorption analyzer, Micromeritics). The sample (100 mg powder catalyst) was firstly activated at 150 °C under 30 mL min^{-1} of He for 30 min. After cooling to 40 °C under He gas, the carrier gas was switched to 5 % H$_2$/Ar (v/v) at 30 mL min^{-1}. When the baseline was stable, the temperature was increased to 900 °C with a ramp of 10 °C min^{-1}. The outlet stream passed through an ice trap to condense water vapor produced during the reduction. The H$_2$ consumption was measured by means of a thermal conductivity detector (TCD).

Temperature programmed desorption of CO$_2$ (CO$_2$-TPD) was performed in an AutoChem II (Chemisorption analyzer, Micromeritics) with 100 mg of catalyst. The catalyst was firstly activated at 150 °C under 30 mL min^{-1} of He for 30 min and then reduced in situ in 5% H$_2$/Ar (v/v) at 30 mL

min^{-1} at 600 $^{\circ}$C (ramp 10 $^{\circ}$C min^{-1}) for 2 h. After cooling down to 40 $^{\circ}$C in He, CO_2 was adsorbed for 1 h with 30 mL min^{-1} of 10 % CO_2/He (v/v). The catalyst was then post-flushed by 30 mL min^{-1} of He for 1 h to remove weakly adsorbed CO_2. The TPD was performed from 40 $^{\circ}$C to 500 $^{\circ}$C in 30 mL min^{-1} of He with a heating rate of 10 $^{\circ}$C min^{-1}. CO_2 signal (m/z = 44) was tracked on a mass spectrometer (MKS, spectra products). CO_2 consumption was calculated using a standard calibration of m/z = 44 conducted on 10 % CO_2/He (v/v). The desorption profile was deconvoluted using Origin 9.0 software.

Diffuse Reflectance for Infrared Fourier Transform Spectroscopy (DRIFTS) measurements were carried out using a Cary 600 Series FTIR Spectrometer (Agilent Technologies) equipped with a Praying Mantis cell by Harrick. The cell size is 4.5 x 3.0 mm (diameter x height), thus its volume is around 47.7 mm^3, which is eight-fold smaller than the catalytic bed volume in the activity test. The conditions during DRIFTS measurements were kept close to those of the catalytic tests in term of gas composition, gas hourly space velocity (GHSV), and experiment protocol. In a typical measurement, the catalyst was initially flushed with He and heated up to 100 $^{\circ}$C to remove possible traces of moisture from the sample or the cell as well as to check the stability of the catalyst. The catalyst was then reduced at 500 $^{\circ}$C (10 $^{\circ}$C min^{-1}) under 20 mL min^{-1} of H_2/He (1:1 v/v). When the reduction step was completed, the H_2 flux was switched off, the sample was then cooled down to target temperature under pure He flow and a single analysis was performed to set a background. A selected gas mixture was eventually introduced to the sample cell depending on the experiment, e.g. 24 mL of 10 % CO_2/He (v/v) and 24 mL of reactants (CO_2/H_2/N_2 = 1/4/1 v/v) for CO_2 adsorption and reaction, respectively. The CO_2 adsorption experiment was performed at 200 $^{\circ}$C while the reactions were carried out from 200 to 325 $^{\circ}$C with a temperature ramp of 10 $^{\circ}$C min^{-1}. A single analysis was composed of 64 scans and lasted 30 s. Several analyses were performed to follow *in situ* the behavior of the catalyst during CO_2 adsorption as well as the reaction.

X-ray photoelectron spectroscopy (XPS) spectra were recorded with a PHI VersaProbe II Scanning XPS Microprobe with scanning monochromatic X-ray Al Kα radiation as the excitation source (200 µm area analysed, 52.8 W, 15kV, 1486.6 eV), and a charge neutralizer. The pressure in analysis chamber was maintained lower than 2.0 x 10^{-6} Pa. High-resolution spectra were recorded at a given take-off angle of 45 ° by a multi-channel hemispherical electron analyser operating in the constant pass energy mode at 29.35 eV. Spectra were charge referenced with the C 1s of adventitious carbon at 284.8 eV. Energy scale was calibrated using Cu 2$p_{3/2}$, Ag 3$d_{5/2}$, and Au 4$f_{7/2}$ photoelectron lines at 932.7, 368.2, and 83.95 eV, respectively.

High resolution transmission electron microscopy (HRTEM) characterization was carried out by a TEM/STEM FEI TECNAI F20 microscope, equipped with an EDS analyzer. Fine powder catalysts were suspended in ethanol under ultrasounds for 20 min. The suspension was subsequently deposited on a Cu grid with lacey quanti-foil carbon film and dried at 100 ºC before doing the measurement. Selected area electron diffraction (SAED) and Fast Fourier transformation (FFT) were applied to determine the interplanar spacing of the crystals. Particle size distribution was processed considering around 150 particles in three different zones for each sample.

Micro-Raman measurements were performed in a Renishaw Raman Invia configured with a Leica DMLM microscope (obj. 5×, 20×, 50×). The available sources are an Ar$^+$ laser (514.5 nm, P_{max} = 30 mW) and a diode-laser (780.0 nm, P_{max} = 300 mW). The system was equipped with edge filters to cut Rayleigh scattering, monochromators (1800 lines/mm for Ar$^+$ laser, and 1200 lines/mm for diode laser) and a Charge-Coupled Device (CCD) thermoelectrically cooled (203 K) detector. Measurements were performed with the Ar$^+$ Laser (514.5 nm) at power level P_{out} = 3 mW (10% power). Each spectrum was recorded by four accumulations (30 s for each).

Ni K-edge X-ray Absorption Fine Structure (XAFS) studies of NiAl and NiLaAl samples were carried out on the B18 beamline at the Diamond Light Source, Didcot, UK. Measurements were performed using a fast-scanning Si (111) double crystal monochromator. All samples were measured

in transmission mode using ion chamber detectors and were diluted with cellulose and pressed into pellets to optimise the effective edge-step of the XAFS data. All transmission XAFS spectra were acquired concurrently with a Ni foil placed between I_t and I_{ref}. The time resolution of the spectra reported herein was 5 min/spectrum ($k_{max} = 14$), on average three scans were acquired to improve the signal to noise level of the data. XAFS data processing and Extended X-ray Absorption Fine Structure (EXAFS) analysis were performed using IFEFFIT [54] (Athena and Artemis) [55]. The amplitude reduction factor, s_0^2, was derived from EXAFS data analysis of known reference compounds (Ni foil) and used as a fixed input parameter.

2.3. CO₂ methanation tests

The tests were performed in a fixed bed quartz reactor (ID 10.0 mm). The powder catalyst (30 mg, 0.420-0.595 mm particle size) diluted with 470 mg quartz with the same particle size was loaded in the reactor. To measure the temperature profile, a 2 mm thermowell (quartz tube) was inserted in the middle of the catalytic bed. The insertion of the thermo-well resulted in height and volume of the catalytic bed around 5 mm and 377 mm^3, respectively. A thermocouple (K-type) was placed inside the thermowell allowing measurement of the temperature along the length of the catalytic bed during the tests. The catalyst was reduced in 200 mL min^{-1} of $H_2/N_2 = 1/1$ (v/v) at 600 °C for 2 h. After cooling down to 225 °C and stabilized at this temperature for 30 min, the feed gas ($CO_2/H_2/N_2 = 1/4/1$ or 1/4/0 v/v) with a total flow rate of 240 mL min^{-1} was sent to the reactor. This condition generated a gas hourly space velocity (GHSV) of around 38,200 h^{-1}, (defined in terms of the total volume of the catalytic bed (inert + catalyst)), or 480 L g_{cat}^{-1} h^{-1} (in terms of the mass of catalyst). The densities of the catalysts were around 1g/mL (NiAl: 1.3; NiLaAl and NiYAl: 1.0; and NiCeAl: 1.7 g/mL). The reaction was carried out from 225 °C to 425 °C with an interval of 25 °C.

After passing through a cold trap for water condensation, the outlet stream was analyzed on-line by a PerkinElmer Autosystem XL gas chromatograph, equipped with two thermal conductivity detectors (TCD) and two Carbo-sphere columns using He as a carrier gas for CO, CH_4 and CO_2 quantification,

and N_2 for H_2 analysis. Since no C_{2+} hydrocarbons were detected, CO_2 conversion, CH_4 and CO selectivities were defined as follows [17]:

$$CO_2 \text{ conversion } (\%) = \frac{[CH_4]+[CO]}{[CH_4]+[CO]+[CO_2]} x100 \qquad (1)$$

$$CO \text{ selectivity } (\%) = \frac{[CO]}{[CH_4]+[CO]} x100 \qquad (2)$$

$$CH_4 \text{ selectivity } (\%) = \frac{[CH_4]}{[CH_4]+[CO]} x100 \qquad (3)$$

In which [A] (A = CH_4, CO, and CO_2) represents for molar ratio of component A in the outlet stream.

For the stability test, the catalyst was challenged under different reaction conditions by 8 cycles of start-up and shut-down the reactor. After testing in diluted gas mixture ($CO_2/H_2/N_2$ = 1/4/1 v/v) at different temperatures from 225 to 425 °C, the reaction was shut down and the catalyst was kept under 100 mL min^{-1} of N_2. In the next three days, the reaction was carried out at 325 °C in diluted gas mixture for 9 h each day. The procedure was repeated in the same way, but the reaction was performed in a concentrated gas mixture ($CO_2/H_2/N_2$ = 1/4/0 v/v).

To ensure a sufficient amount of used catalyst for post reaction XAFS measurement, the test was also performed with 120 mg of catalyst (keeping the same GHSV as in the test with 30 mg by decreasing the amount of quartz (diluent)) at four set points of oven temperature at 225 – 300 °C. Temperatures similar to those in stability tests, e.g. maximum temperature of 439 °C at T_{oven} = 300 °C) were reached.

3. Results and discussion

3.1. Powder Ni-containing hydrotalcite precursors and catalysts

The crystallinity of the layered NiAl HT structure, intercalated with carbonates, decreases by the addition of rare-earth elements. Less intense and broader basal (003) and (006) reflections and overlapped (110) and (113) reflections are recorded in NiLaAl than in NiAl precursors (Fig. S1a), due to a lower order in the stacking direction and within the layers. The larger size of La^{3+} leads to

the formation of $La_2(CO_3)_2(OH)_2$ [45]. A similar cubic CeO_2 phase separation occurs for the large Ce^{4+} ion [56], while Y^{3+} could be included into the brucite-type layers of the HT structure, distorting the lamellar structure [57].

The catalysts have been characterized after calcination at 600 °C. Note that the data presented in the main manuscript focusses on La-containing catalysts whereas information concerning Ce and Y-containing samples is located in the supplementary information. The catalysts are made by nano-crystalline NiAl mixed oxides (Fig. 1, S1b) with NiO crystallite sizes in the 3.1 – 4.4 nm range, Table 1. La^{3+} is observed to segregate as La_2O_3 and is seen to decrease the crystallite size of the NiO (Table 1). Making a comparison with Y and Ce-samples, Y also helps to decrease the NiO crystallite size, while the oxide is unmodified by the segregated CeO_2. This behavior could be related to a higher dispersion of La_2O_3 in the oxide; however, the inclusion of La^{3+} into the mixed oxide structure cannot be discarded. BET surface areas of NiAl and NiLaAl catalysts are 159 and 149 $m^2\,g^{-1}$ respectively (Table 1). The differences in the values could be related to different types of pores in the samples (Fig. S2, N_2 isotherm) rather than to the segregation of La_2O_3. Indeed, taking into account also the surface areas of Y and Ce-samples the values do not correlate well with the composition and crystallinity of the catalysts. Micro-Raman spectra indicate the formation of nano NiO with a high nickel vacancy concentration in all the catalysts (Fig. S3); this kind of oxide gives rise to an intense band at 550 cm^{-1}, due to the one-phonon LO (longitudinal optical) mode, and a broad band at 1100 cm^{-1}, attributed to a two-phonon 2LO mode [58, 59].

XPS spectra give further information about defects on the surface of the catalysts. In the Ni $2p$ core level XPS spectra (Fig. 2a, Fig. S4), the binding energy (B.E.) values of the main peak at 855.4-855.7 eV are in between of those of NiO and $NiAl_2O_4$, which is characteristic of Ni^{2+} in NiAl HT-derived mixed oxides [60]. The main Ni $2p_{3/2}$ peaks are broadened in comparison to pure NiO, a feature less remarkable for the NiLaAl catalyst (Fig. S4 and Table 2). This behavior is due to the merging of the main peak and the satellite I (Sat I), assigned to defects such as Ni^{3+} species [61, 62],

Ni^{2+} vacancies or Ni^{2+}-OH sites [63], and satellite 2 (Sat 2) due to ligand- metal charge transfer [63-65]. The binding energy value for La 3$d_{5/2}$ at 834.9 eV is typical of La^{3+} species; similarly, the Ce 3$d_{5/2}$ and Y 3$d_{5/2}$ binding energy values at 879.5 eV and 157.4 eV are related to Ce^{4+} and Y^{3+} [66]. On the other hand, the O 1s core level spectra of all the catalysts show a clear shift at high binding energy with respect to O 1s core level spectrum of the reference NiO (Fig. 2b). These O 1s signals can be deconvoluted into two contributions, giving information about the nucleophilic and electrophilic character of the oxygen species [62, 67]. The contribution due to nucleophilic lattice oxygen (i.e. O^{2-}) at 530.0 eV is more intense than the signal at 531.8 eV due to electrophilic surface oxygen species (likely O^{-} or adsorbed O^{2-}), but the relative intensities of both contributions are not significantly modified with the incorporation of rare-earth elements (Table 2). The observed Al 2p binding energy values, spectra not shown, at 73.5-74.0 eV are typical of Al^{3+} ions in all cases [66]. The promotion effect of rare-earth elements is also clear from the surface Ni/Al atomic ratio values (Table 2). These surface ratios increase from 2.30 for sample NiAl to 2.91 for sample NiLaAl indicating a higher dispersion of the nickel oxide in the latter. This behaviour could be related to the different ionic radius of the cations (0.116, 0.097 and 0.096 nm for La^{3+}, Ce^{4+} and Y^{3+}, respectively). The higher the ionic radius, the higher the surface Ni/Al atomic ratio.

Conversely, the reduction temperature of nickel species, investigated by H$_2$-TPR, is not significantly modified with the addition of La or the other rare-earth elements (Fig. 3 and Fig. S5). The calcination of HT precursors at 600 °C generates Ni species well dispersed and stabilized by the mixed oxide and therefore reduced from 450 °C to 850 °C with the main reduction event taking place at ca. 750 °C. The reduction temperature is dependent on the parameters of the H$_2$-TPR experiments and calcination temperature, see further details about the reducibility of the samples in the supplementary information (Fig. S6). An attempt was made to investigate the catalyst reducibility from H$_2$-TPR data (Table S1), The estimated H$_2$ reducibility degree is larger for NiAl than for rare-earth containing catalysts; nevertheless, unquantified defects in the samples or the reducibility of

CeO_2 in NiCeAl makes it rather difficult to correlate H_2 consumption and nickel species reducibility [68]. To obtain more information about the reducibility of the samples after activation prior to catalytic tests, the calcined catalyst was reduced in the reactor and characterized *ex situ* by XRD. The Ni^0 metallic reflections develop and only very broad and poor intense reflections due to NiO are observed (Fig. S7), which could be also due to the oxidation of Ni^0 in contact with the atmosphere (vide characterization of spent catalysts).

The basicity of the reduced catalysts, investigated by CO_2-TPD (Fig. 4, Fig. S8 and Table 3), can be understood in terms of weak (OH^-), medium (acid-base lewis pairs) and strong (O_2^-) basic sites that bind bicarbonate, bidentate and monodentate carbonate respectively [50, 69, 70]. The total amounts of CO_2 adsorbed per gram of catalyst are larger for the La sample (ergo, it possesses a higher basicity) followed by Y and Ce-promoted samples. The sites that bind bidentate carbonate comprise the main contribution to the CO_2 adsorption, and rare-earth elements (specially La) have a higher impact on the formation of sites that bind monodentate carbonate, reported as the most active for the CO_2 methanation [19]. These basic properties could be related to the basicity of the pristine rare-earth oxides, which has been previously reported to vary according to the following order: $La_2O_3 > Y_2O_3 >> CeO_2$ [71], and which has been proposed to depend on the radius of the cation and the nature of crystalline phases. It is however expected that the surface area and dispersion of the rare-earth oxides in the matrix may also play a role in modifying the basic properties [72].

3.2. Catalytic activity

Rare-earth elements greatly enhance the activity at oven temperatures below 300 °C (in the kinetic-limited region), while differences are less remarkable with rising the temperature because of the thermodynamic limitations, see Fig. 5. The maximum conversion (and oven temperature to reach it) is seen to depend on the catalyst; the NiLaAl catalyst is the most active over the whole temperature range, followed by NiCeAl and NiYAl catalysts (except for 250 °C where Y > Ce). Note however that the Ni loading on the rare-earth catalysts is 6-8 wt.% lower than that in NiAl (Table 1).

14

Selectivities to CO are also related to the activity, for instance the NiLaAl catalyst shows a CO selectivity 3.1 % at T_{oven} = 325 ºC, lower than for the NiAl catalyst (CO selectivity = 7.2 %). At 425 ºC the contribution of the Reverse Water-Gas Shift (RWGS) is responsible for the increase in CO selectivity up to ca. 10 %.

NiLaAl has an outstanding performance in particular at only 250 °C (64 % CO_2 conversion with a 98 % selectivity to CH_4), taking into account the high space velocity value. Indeed, a CO_2 conversion of 88 % with almost exclusive production of CH_4 (selectivity > 99 %) could be achieved by loading 4 times the NiLaAl catalyst amount (i.e. 120 mg instead of 30 mg) whilst keeping the total volume of the bed and feed flow constant (Fig. S9); however, the temperature inside the catalytic bed should be considered (vide infra). The low selectivities to CO for promoted catalysts at the higher space velocity values used in this work, together with the small difference in CO produced by decreasing the space velocity value in NiLaAl tests, suggest that the CO methanation limiting-step previously proposed in the literature [73] does not have a remarkable effect over the high Ni-loaded catalysts investigated here.

Notwithstanding the high degree of dilution of the catalyst in the bed, which reduces the local volumetric activity of the catalysts, the temperature profiles measured in the centerline of the bed (Fig. S10) demonstrate that, even at conversions lower than 10 %, it is not possible to achieve an isothermal temperature. It should be noted that heat losses due to radiation and/or convection may occur. The temperature increases along all catalytic beds and reaches the maximum in the latter part of the bed due to the high space velocity applied [3, 52, 74]. Temperature gradients are not only related to the type of catalyst (the better activity, the higher temperature) but also to the set temperature (Fig. 6a). Setting an oven temperature higher than 325 ºC renders the effect of the temperature increment less significant, whereas the CO_2 conversion decreases only slightly, most likely due to the contribution of the endothermic RWGS reaction. By increasing the catalyst/dilutant ratio (loading 120 mg of catalyst instead of 30 mg), a higher temperature increase is recorded, e.g. at

$T_{oven} = 250\,°C$ it is ca. 161 °C, these higher temperatures in the catalytic bed foster the CO_2 conversion previously commented.

A thermal positive feedback exists far from the thermodynamic equilibrium, i.e. an increase in local temperature tends to increase the reaction rate, which in turn tends to increase local temperature [75, 76]. Hence, to better compare among catalysts, CO_2 conversions are plotted against outlet temperature and compared to thermodynamic equilibrium data (Fig. 6b). The activity order is always La > Ce > Y > NiAl, and the equilibrium is only reached at temperatures above 450 °C. This behavior confirms that the order in the reported catalytic activity is not an artifact of the temperatures developed in the reactor.

The productivity of the catalysts in term of the rate of volume of CH_4 formation per mass unit of Ni used is summarized in Table 1. The results confirm that the La-containing sample achieves the highest productivity (101 L g^{-1} h^{-1}). In comparison with Ni catalysts reported in the literature (Table S2), our catalysts show outstanding properties. Productivities here obtained are 3-5 fold higher than those obtained with Ni/La_2O_3, Ni/CeO_2, Ni/PrO_x [34], $Ni/CaO-Al_2O_3$ [16], $Ni-La/Al_2O_3$ [31], $NiWMgO_x$ [77] catalysts at atmospheric pressure or Ni_3Fe/Al_2O_3 [16] at 6 bar. The productivities are only slightly lower than those for $Ni/Fe-Al_2O_3$ [40], $NiMnAlO_x$ and $NiFeO_x$ [41] catalysts operating at 5 and 8 bar, namely under thermodynamically favored conditions.

The tests performed over the NiLaAl catalyst under transient conditions in Fig. 7 show that both CO_2 conversion and CH_4 selectivity are very stable (71.7 ± 0.5% and 97.3 ± 0.1%, respectively) during the first 33 h of TOS in the $CO_2/H_2/N_2 = 1/4/1$ v/v feedstock at $T_{oven} = 325\,°C$ ($T_{max} = 440\,°C$) and three shut-down (to room temperature) and start-up cycles. In the following N_2-free tests, activity is slightly higher at the beginning (CO_2 conversion = 72.5 ± 0.4 %, selectivity in CH_4 = 96.9 ± 0.1 %), as the partial pressures and temperature increase in the bed (10 – 15 °C higher than in diluted mixtures $T_{max} = 455\,°C$, Fig. 8a, b). The performance only slightly decreases with time. The constant conversions and selectivities are accompanied by stable temperature profiles along the length of the

16

catalytic bed (Fig. 8c, d). Remarkably, the temperature inside the bed reaches values close to 460 °C, a temperature that has previously been reported to be similar to that reached by a hot spot in a methanation reactor [78]. As such this allows us to assess the stability of these catalysts under harsh reaction conditions. To further check the stability of the NiLaAl catalysts, 8 h tests at T_{oven} =325 °C are repeated in addition to obtaining an activity curve from 225 to 425 °C. Since there are no differences in the activity curves and temperature profiles, especially at low temperatures, we determine the catalysts to be stable.

3.3. Spent catalysts and structure/activity relationship

Carbon formation and laydown by Bouduart reaction is ruled out by micro-Raman analyses (Fig. S11), in agreement with previous results [38, 42, 79]. The presence of reflections pertaining to Ni^0 in the diffraction patterns (Fig. 1 and Fig. S1b) suggests that catalysts remain fully reduced after tests, although surface oxidation by exposure to the air during handling cannot be discarded. Ni^0 crystallite size decreases for La-sample in comparison to NiAl (Table 1); a similar effect is observed for the Y-catalyst. Ni particles are deposited on and embedded in aggregates of ill-shaped nanometric catalyst particles (Fig. 9 and Fig. S12). The Ni particle size distribution ranges from 1.0 to 8.0 nm for NiLaAl catalyst, with a mean size determined to be around 4.1 nm (Fig. 9b1). In contrast for NiAl, particles up to 12.0 nm are observed with a mean size of ca. 4.9 nm (Fig. 9a1). NiYAl catalyst also retains a small Ni^0 particle size (~ 4.4 nm according to XRD), whilst Ce-sample behaves like the unpromoted NiAl catalyst (i.e. larger particles form ~ 6 nm in size) (Fig. S12). Diffraction rings related to both Ni^0 and NiO phases in SAED analysis evidence surface oxidation of Ni^0 particles (Fig. S13).

The trend in Ni^0 crystallite size is similar to that seen for the for NiO in calcined catalysts (Table 1), notwithstanding that the NiLaAl catalyst was reacted for a longer TOS (66 h) than the other catalysts (~16 h). These results indicate that the Ni^0 particles after reduction and tests in high loaded HT-derived catalysts remain stable, which is further confirmed by HRTEM. On first glance, the smaller Ni particle size of the La-containing catalyst in comparison to NiAl could explain its higher

activity. However, the smallest Ni^0 particles are observed in the Y-containing catalyst which does not possess the best activity. Thus, even at the high Ni-loadings used in this work, a trade-off between available Ni^0 particle size and basicity (and therefore activation of CO_2 on the support) seems to be necessary. It should be remembered that the basicity follows the order: NiLaAl > NiYAl > NiAl. The promoting effect of Ce is neither related to the Ni^0 particle size nor to the basicity. The Ni^0 particle size in NiCeAl is similar to that seen for the NiAl catalyst, while the basicity is lower than for NiLaAl (Table 3). In this catalyst, the CeO_x support, in particular partially reduced CeO_2 (Ce^{3+}/Ce^{4+}), may play a key role in the O abstraction from CO_2 [80]. A further investigation on the effect of Ce on the activity is out of the scope of this work.

3.4. The effect of La on NiLaAl catalysts

To go insight into the effect of La on the catalyst XAFS measurements were performed on NiAl and NiLaAl samples. Fig. 10a shows the XANES spectra of NiAl and NiLaAl calcined samples. A comparison with the absorption edge of the Ni foil and NiO reference samples clearly indicates that the NiO is present and is therefore consistent with the observations made from XRD and that La does not modify the structure of the NiO phase. This may suggest that the Sat 1 observed in XPS is mainly related to Ni^{2+} vacancies, (note that this is consistent with the black coloration of the samples [81]). The Fourier transform (FT) of the EXAFS also supports this with peaks at ~ 2 and 3 Å in the phase uncorrected data, corresponding to Ni-O and Ni-Ni in NiO respectively for the catalysts (Fig. 10b). This contrasts with the Ni foil which has a sharp peak at ~ 2.5 Å due to fit shell metallic Ni-Ni distances. Hence, in the HT-derived catalysts calcined at 600 °C here investigated, La does not change the interaction between Ni and the matrix. Indeed STEM/EDS element distribution maps of used NiLaAl catalyst (Fig. 9b2) show that Ni particles are distributed across both Al and La support elements indicating that La exists as separate, well-distributed nano La_2O_3 domains in agreement with XPS data. This behavior is somewhat different to that seen in ref [32], where La was observed to change the interaction between Ni and periclase, this behavior being related to differences in La

content (5.0 vs 1.5 at.%), composition of the HT (NiAl vs NiMgAl) and reduction temperature (600 vs 900 °C).

After reaction the XANES spectra changes from being typical of NiO to more closely matching that of the Ni foil (Fig. 10c), indicating the catalyst has been reduced. This can be seen by the increase in the pre-edge intensity at ~ 8340 eV and a lower rising absorption edge intensity at 8355 eV. The intensity of both features is however in between that of the oxide and metal forms suggesting a mixture of the two states. Interestingly, this is not necessarily borne out in the FT (Fig. 10d) which shows essentially the complete disappearance of the Ni-O and Ni-Ni distances of the pre-reaction calcined catalysts, shown in Fig. 10b. These peaks are replaced by a first shell metallic Ni-Ni at ~2.5 Å, as well as matching the foil for higher shells albeit with lower intensity. Although the Fourier transform intensity is less than the foil for the used catalyst this could be explained by particle size effects and almost certainly due to there being a component of NiO still present (which could be also related to the oxidation by exposure to air during catalyst handling). A subsequent linear combination fitting of the XANES with Ni-metal and NiO was performed in two manners: firstly, by forcing the program to obtain a weighted sum of the two standards' functions (Ni-metal and NiO) to be equal to one and not. Below are reported the results when the program was forced (fitting done using as limit 20 eV below and 50 eV above the edge jump). As it can be seen from Table 4, the amounts present of the oxide and metal components reflect the observations in the XANES and is suggestive of the presence of primarily, Ni metal in both samples. Interestingly the Ni environment in the sample containing La is more reduced when compared to that without.

The interaction of CO_2 with NiAl and NiLaAl was studied by CO_2-DIRIFTs both feeding only CO_2 and under reaction conditions. DRIFTs spectra recorded over NiAl and NiLaAl feeding CO_2 at 200 °C in Fig. 11 demonstrate that the activation of CO_2 on the surface occurs by both dissociative (CO_{ads} on Ni^0 particles) and associative (formation bicarbonate and carbonate on the support) pathways. Interestingly, La modifies the CO_2 interaction with the catalysts. For NiAl (Fig. 11a), CO_2

is firstly activated on Ni^0 particles forming CO adsorbed on linear (2030 cm^{-1}), bridged (1930 cm^{-1}) and three-fold (1868 cm^{-1}) configurations [38]. Afterwards, CO_2 also interacts with the support and bands are recorded in the O-C-O stretching region due to CO_2 associatively activated over weak, medium and strong basic sites (previously identified by CO_2-TPD) as bicarbonate (1631, 1440 and 1215 cm^{-1}), bidentate (1584, 1334-1295 cm^{-1}) and monodentate carbonate (1526 and 1395 cm^{-1}), respectively [19, 50]. Conversely, for NiLaAl, CO_2 seems to be simultaneously activated on both Ni^0 and the support, resulting in the formation of both carbonyl and bicarbonate/carbonate bands in Fig. 11b. This suggests a stronger interaction of CO_2 with the support on NiLaAl than on NiAl catalyst; we note that DRIFTS measurements are not typically used for obtaining quantitative information on adsorption behavior, however the results observed here show a clear trend with catalytic performance, especially the nature of the adsorbed species are similar for both types of catalysts.

CO_2 hydrogenation is quite fast, once H_2 is added to the CO_2 feed at 200 °C (Fig. 12), the bands of reaction intermediates are significantly modified and CH_4 evolves (1305 cm^{-1}). Bicarbonate and monodentate carbonate species are hydrogenated to formates at temperatures between 200 - 250 °C [19], prompting a decrease in intensity of 1631 and 1395 cm^{-1} bands and the simultaneous increase of the O-C-O and C-H formate bands at 1584 and 2840 cm^{-1}, respectively. Moreover, the band at around 1215 – 1220 cm^{-1} assigned to bicarbonate (Fig. 12b and 12d) almost completely vanishes during reaction even at low temperature 200 °C, suggesting that it is easily transformed. The higher intensity of the 2840 cm^{-1} band for NiLaAl sample (Fig. 12c) implies a higher contribution of the associative mechanism over this catalyst, which may explain its higher activity at lower temperatures. The shape of the spectrum also changes in the Ni-CO vibrations region as soon as H_2 is co-fed; peaks due to C-O stretching of bridged and three-folded CO on Ni^0 become more intense for example (see further details in Fig S14). At around 250 °C, the high amount of water produced, particularly for the more active NiLaAl catalyst, results in a very intense background, rendering it difficult to accurately evaluate the bands, although the presence of bidentate carbonates can be still confirmed.

4. Summary and conclusions

A bulk high-loaded Ni-based catalyst promoted by La is easily prepared by coprecipitation of a hydrotalcite-type compound and its calcination at moderate temperatures. The NiLaAl catalyst shows an outstanding CH_4 productivity (101 $L_{methane}$ g_{Ni}^{-1} h^{-1}) and stability after 66 h of TOS in diluted and concentrated gas mixtures and shut-down/start-up cycles. The performance can be correlated to the presence of nano-La_2O_3 patches in the NiAl mixed oxide matrix that increase the catalyst basicity and decrease the NiO_x crystallite size and in turn lead to the formation small ($\sim 4 - 5$ nm) and well dispersed Ni^0 particles. Consequently, the catalyst promotes both an associative and dissociative pathway, resulting in a significant activity enhancement in comparison to the unpromoted NiAl sample. Remarkably, Ce and Y have less marked effect on the activity improvement (NiLaAl > NiCeAl $\approx$ NiYAl > NiAl). Patches of CeO_2 do not alter the crystallite size and lead to a lower increase in the basicity, however, in this case the role of Ce^{3+}/Ce^{4+} should be considered. Whilst Y, which could be incorporated into the mixed oxide, results in a smaller crystallite size, comparable to La, but the catalyst possesses a lower basicity. These results underly the importance of a trade-off between Ni^0 particle size and basicity (Table S3). Though temperature profiles along the centre line of the bed evidence that the heat developed by the exothermic reaction should be considered in order to evaluate the activity of highly active catalysts even if diluted with inert material in the bed.

Hence, the presence of basic oxides segregated on the Al_2O_3 support could be a future strategy for improving the performance of CO_2 methanation catalysts. The activity of the catalysts could be further optimized by decreasing both Ni and basic oxide particle sizes to improve their dispersions and in turn their mixing and therefore the promotion effect.

respectively. We also acknowledge XAFS measurements performed through the UK Catalysis Hub BAG access.

References

[1] E. Giglio, A. Lanzini, M. Santarelli, P. Leone, Synthetic natural gas via integrated high-temperature electrolysis and methanation: Part I—Energy performance, J. Energy Storage 1 (2015) 22−37, https://doi.org/10.1016/j.est.2015.04.002.

[2] M. Therma, F. Bauer, M. Sterner, Power-to-Gas: Electrolysis and methanation status review, Renew. Sust. Energ. Rev. 112 (2019) 775 – 787, https://doi.org/10.1016/j.rser.2019.06.030.

[3] D. Türks, H. Mena, U. Armbruster, A. Martin, Methanation of CO_2 on Ni/Al_2O_3 in a Structured Fixed-Bed Reactor—A Scale-Up Study, Catalysts 7 (2017) 152, https://doi.org/10.3390/catal7050152.

[4] S. Rönsch, J. Schneider, S. Matthischke, M. Schlüter, M. Götz, J. Lefebvre, P. Prabhakaran, S. Bajohr, Review on methanation – From fundamentals to current projects, Fuel 166 (2016) 276–296, https://doi.org/10.1016/j.fuel.2015.10.111.

[5] N. Gallandat, R. Mutschler, V. Vernay, H. Yang, A. Züttel, Experimental performance investigation of a 2 kW methanation reactor, Sustain. Energ. Fuels 2 (2018) 1101-1110, https://doi.org/10.1039/C8SE00073E.

[6] C. Bassano, P. Deiana, L. Lietti, C.G. Visconti, P2G movable modular plant operation on synthetic methane production from CO_2 and hydrogen from renewables sources, Fuel 253 (2019) 1071-1079, https://doi.org/10.1016/j.fuel.2019.05.074.

[7] T. Chwoła, T. Spietz, L. Więcław-Solny, A. Tatarczuk, A. Krótki, S. Dobras, A. Wilk, J. Tchórz, M. Stec, J. Zdeb, Pilot plant initial results for the methanation process using CO_2 from amine scrubbing at the Łaziska power plant in Poland, Fuel, 263 (2020) 116804, https://doi.org/10.1016/j.fuel.2019.116804.

[8] M. Bailera, P. Lisbona, L.M. Romeo, S. Espatolero, Power to Gas projects review: Lab, pilot and demo plants for storing renewable energy and CO_2, Renew. Sust. Energ. Rev. 69 (2017) 292-312. https://doi.org/10.1016/j.rser.2016.11.130.

[9] Clariant supplies SNG catalyst for first commercial CO_2 methanation plant. https://www.clariant.com/en/Corporate/News/2013/10/Clariant-Supplies-SNG-Catalyst-for-First-Commercial-CO2-Methanantion-Plant, 2013 (accessed 9 June 2020).

[10] World's Largest SNG Plant Goes On-Stream in China with Catalysts and Process Technology from Haldor Topsoe A/S. https://blog.topsoe.com/worlds-largest-sng-plant-goes-stream-china-catalysts-and-process-technology-haldor-topsoe#:~:text=Today%20Haldor%20Topsoe%20A%2FS,the%20northwestern%20part%20of%20China, 2013 (accessed 9 June 2020).

[11] K.P. Brooks, J. Hu, H. Zhu, R.J. Kee, Methanation of carbon dioxide by hydrogen reduction using the Sabatier process in microchannel reactors, Chem. Eng. Sci. 62 (2007) 1161 – 1170, https://doi.org/10.1016/j.ces.2006.11.020.

[12] D. Sun, F.M. Khan, D.S.A. Simakov, Heat removal and catalyst deactivation in a Sabatier reactor for chemical fixation of CO_2: Simulation-based analysis, Chem. Eng. J. 329 (2017) 165–177, https://doi.org/10.1016/j.cej.2017.06.160.

[13] J.R. Rostrup-Nielsen, K. Pedersen, J. Sehested, High temperature methanation: Sintering and structure sensitivity, Appl. Catal. A Gen. 330 (2017)134–138, https://doi.org/10.1016/j.apcata.2007.07.015.

[14] A. Quindimil, U. De-La-Torre, B. Pereda-Ayoa, A. Davó-Quiñonero, E. Bailón-García, D. Lozano-Castelló, J. A. González-Marcos, A. Bueno-López, J.R. González-Velasco, Effect of metal loading on the CO_2 methanation: A comparison between alumina supported Ni and Ru catalysts, Catal. Today, in press, https://doi.org/10.1016/j.cattod.2019.06.027.

[15] C. Vogt, E. Groeneveld, G. Kamsma, M. Nachtegaal, L. Lu, C.J. Kiely, P.H. Berben, F. Meirer, B.M. Weckhuysen, Unravelling structure sensitivity in CO_2 hydrogenation over nickel, Nat. Catal. 1 (2018) 127–134, https://doi.org/10.1038/s41929-017-0016-y.

[16] B. Mutz, M. Belimov, W. Wang, P. Sprenger, M.A. Serrer, D. Wang, P. Pfeifer, W. Kleist, J.D. Grunwaldt, Potential of an Alumina-Supported Ni_3Fe Catalyst in the Methanation of CO_2: Impact of Alloy Formation on Activity and Stability, ACS Catal. 7 (2017) 6802–6814, https://doi.org/10.1021/acscatal.7b01896.

[17] H. Muroyama, Y. Tsuda, T. Asakoshi, H. Masitah, T. Okanishi, T. Matsui, K. Eguchi, Carbon dioxide methanation over Ni catalysts supported on various metal oxides, J. Catal. 343 (2016) 178–184, https://doi.org/10.1016/j.jcat.2016.07.018.

[18] D. Beierlein, D. Häussermann, M. Pfeifer, T. Schwarz, K. Stöwe, Y. Traa, E. Klemm, Is the CO_2 methanation on highly loaded $Ni-Al_2O_3$ catalysts really structure-sensitive?, Appl. Catal. B Environ. 247 (2019) 200–219, https://doi.org/10.1016/j.apcatb.2018.12.064.

[19] Q. Pan, J. Peng, T. Sun, S. Wang, S. Wang, Insight into the reaction route of CO_2 methanation: Promotion effect of medium basic sites, Catal. Commun. 45 (2014) 74–78, https://doi.org/10.1016/j.catcom.2013.10.034.

[20] L. He, Q. Lin, Y. Liu, Y. Huang, Unique catalysis of Ni-Al hydrotalcite derived catalyst in CO_2 methanation: cooperative effect between Ni nanoparticles and a basic support, J. Energ. Chem. 23 (2014) 587–592, https://doi.org/10.1016/S2095-4956(14)60144-3.

[21] P.A.U. Aldana, F. Ocampo, K. Kobl, B. Louis, F. Thibault-Starzyk, M. Daturi, P. Bazin, S. Thomas, A.C. Roger, Catalytic CO_2 valorization into CH_4 on Ni-based ceria-zirconia. Reaction mechanism by operando IR spectroscopy, Catal. Today 215 (2013) 201–207, https://doi.org/10.1016/j.cattod.2013.02.019.

[22] W. Ahmad, M.N. Younis, R. Shawabkeh, S. Ahmed, Synthesis of lanthanide series (La, Ce, Pr, Eu & Gd) promoted $Ni/\gamma-Al_2O_3$ catalysts for methanation of CO_2 at low temperature under

atmospheric pressure, Catal. Commun. 100 (2017) 121–126, https://doi.org/10.1016/j.catcom.2017.06.044.

[23] E.D. Rivero-Mendoza, J.N.G. Stanley, J. Scott, K.F. Aguey-Zinsou, An Alumina-Supported Ni-La-Based Catalyst for Producing Synthetic Natural Gas, Catalysts 6 (2016) 170, https://doi.org/10.3390/catal6110170.

[24] M. Ding, J. Tu, Q. Zhang, M. Wang, N. Tsubaki, T. Wang, L. Ma, Enhancement of methanation of bio-syngas over CeO_2-modified Ni/Al_2O_3 catalysts, Biomass Bioenerg. 85 (2016) 12–17, https://doi.org/10.1016/j.biombioe.2015.11.025.

[25] S.V. Moghaddam, M. Rezaei, F. Meshkani, R. Daroughegi, Carbon dioxide methanation over $Ni-M/Al_2O_3$ (M: Fe, CO, Zr, La and Cu) catalysts synthesized using the one-pot sol-gel synthesis method, Int. J. Hydrog. Energy 43 (2018) 16522-16533, https://doi.org/10.1016/j.ijhydene.2018.07.013.

[26] L. Xu, F. Wang, M. Chen, D. Nie, X. Lian, Z. Lu, H. Chen, K. Zhang, P. Ge, CO_2 methanation over rare earth doped Ni based mesoporous catalysts with intensified low-temperature activity, Int. J. Hydrog. Energy 42 (2017) 15523–15539, https://doi.org/10.1016/j.ijhydene.2017.05.027.

[27] J. Guilera, J. del Valle, A. Alarcón, J.A. Díaz, T. Andreu, Metal-oxide promoted Ni/Al_2O_3 as CO_2 methanation micro-size catalysts, J. CO_2 Utiliz. 30 (2019) 11–17, https://doi.org/10.1016/j.jcou.2019.01.003.

[28] S. Rahmani, F. Meshkani, M. Rezaei, Preparation of Ni-M (M: La, Co, Ce, and Fe) catalysts supported on mesoporous nanocrystalline γ-Al_2O_3 for CO_2 methanation, Environ. Progress Sust. Energy 38 (2019) 118–126. https://doi.org/10.1002/ep.13040.

[29] A. Alarcón, J. Guilera, J.A. Díaz, T. Andreu, Optimization of nickel and ceria catalyst content for synthetic natural gas production through CO_2 methanation, Fuel Process. Technol. 193 (2019) 114–122, https://doi.org/10.1016/j.fuproc.2019.05.008.

[30] W. Gac, W. Zawadzki, M. Rotko, G. Słowik, M. Greluk, CO_2 Methanation in the Presence of Ce-Promoted Alumina Supported Nickel Catalysts: H_2S Deactivation Studies, Top. Catal. 62 (2019) 524-534, https://doi.org/10.1007/s11244-019-01148-3.

[31] G. Garbarino, C. Wang, T. Cavattoni, E. Finocchio, P. Riani, M. Flytzani-Stephanopoulos, G. Busca, A study of $Ni/La-Al_2O_3$ catalysts: A competitive system for CO_2 methanation, Appl. Catal. B Environ. 248 (2019) 286-297, https://doi.org/10.1016/j.apcatb.2018.12.063.

[32] D. Wierzbicki, R. Baran, R. Dębek, M. Motak, M.E. Gálvez, T. Grzybek, P. Da Costa, P. Glatzel, Examination of the influence of La promotion on Ni state in hydrotalcite-derived catalysts under CO_2 methanation reaction conditions: Operando X-ray absorption and emission spectroscopy investigation, Appl. Catal. B Environ. 232 (2018) 409-419. https://doi.org/10.1016/j.apcatb.2018.03.089.

[33] A. Alarcón, J. Guilera, R. Soto, T. Andreu, Higher tolerance to sulfur poisoning in CO_2 methanation by the presence of CeO_2, Appl. Catal. B Environ. 263 (2020) 118346. https://doi.org/10.1016/j.apcatb.2019.118346.

[34] V. Alcalde-Santiago, A. Davó-Quiñonero, D. Lozano-Castelló, A. Quindimil, U.I De-La-Torre, B. Pereda-Ayo, J.A. González-Marcos, J.R. González-Velasco, A. Bueno-López, $Ni/LnOx$ Catalysts (Ln=La, Ce or Pr) for CO_2 Methanation, ChemCatChem 11 *(*2019) 810–819, https://doi.org/10.1002/cctc.201801585.

[35] A. Cárdenas-Arenas, A. Quindimil, A. Davó-Quiñonero, E. Bailón-García, D. Lozano-Castelló, U. De-La-Torre, B. Pereda-Ayo, J.A. González-Marcos, J.R. González-Velasco, A. Bueno-López, Isotopic and in situ DRIFTS study of the CO2 methanation mechanism using Ni/CeO_2 and Ni/Al_2O_3 catalysts, Appl. Catal. B Environ. 265 (2020) 118538. https://doi.org/10.1016/j.apcatb.2019.118538.

[36] C. Italiano, J. Llorca, L. Pino, M. Ferraro, V. Antonucci, A. Vita, CO and CO_2 methanation over Ni catalysts supported on CeO_2, Al_2O_3 and Y_2O_3 oxides, Appl. Catal. B Environ. 264 (2020) 118494, https://doi.org/10.1016/j.apcatb.2019.118494.

[37] S. Abate, C. Mebrahtu, E. Giglio, F. Deorsola, S. Bensaid, S. Perathoner, R. Pirone, G. Centi, Catalytic Performance of γ-Al$_2$O$_3$–ZrO$_2$–TiO$_2$–CeO$_2$ Composite Oxide Supported Ni-Based Catalysts for CO$_2$ Methanation, Ind. Eng. Chem. Res. 55 (2016) 4451-4460, https://doi.org/10.1021/acs.iecr.6b00134.

[38] S. Ewald, M. Kolbeck, T. Kratky, M. Wolf, O. Hinrichsen, On the deactivation of Ni-Al catalysts in CO$_2$ methanation, Appl. Catal. A Gen. 570 (2019) 376-386, https://doi.org/10.1016/j.apcata.2018.10.033.

[39] S. Rahmani, M. Rezaei, F. Meshkani, Preparation of highly active nickel catalysts supported on mesoporous nanocrystalline γ-Al$_2$O$_3$ for CO$_2$ methanation, J. Ind. Eng. Chem. 20 (2014) 1346–1352, https://doi.org/10.1016/j.jiec.2013.07.017.

[40] C. Mebrahtu, S. Abate, S. Chen, A.F. Sierra Salazar, S. Perathoner, F. Krebs, R. Palkovits, G. Centi, Enhanced Catalytic Activity of Iron-Promoted Nickel on γ-Al$_2$O$_3$ Nanosheets for Carbon Dioxide Methanation, Energy Technol. 6 (2018) 1196–1207, https://doi.org/10.1002/ente.201700835.

[41] T. Burger, F. Koschany, O. Thomys, K. Köhler, O. Hinrichsen, CO$_2$ methanation over Fe- and Mn-promoted co-precipitated Ni-Al catalysts: Synthesis, characterization and catalysis study, Appl. Catal. A Gen. 558 (2018) 44-54, https://doi.org/10.1016/j.apcata.2018.03.021.

[42] C. Mebrahtu, S. Perathoner, G. Giorgianni, S. Chen, G. Centi, F. Krebs, R. Palkovits, S. Abate, Deactivation mechanism of hydrotalcite-derived Ni–AlOx catalysts during low-temperature CO$_2$ methanation via Ni-hydroxide formation and the role of Fe in limiting this effect, Catal. Sci. Technol. 9 (2019) 4023-4035, https://doi.org/10.1039/C9CY00744J.

[43] D. Wierzbicki, M. Motak, T. Grzybek, M.E. Gálvez, P. Da Costa, The influence of lanthanum incorporation method on the performance of nickel-containing hydrotalcite-derived catalysts in CO$_2$ methanation reaction, Catal. Today 307 (2018) 205-211, https://doi.org/10.1016/j.cattod.2017.04.020.

[44] L. Zhang, L. Bian, Z. Zhu, Z. Li, La-promoted Ni/Mg-Al catalysts with highly enhanced low-temperature CO_2 methanation performance, Int. J. Hydrog. Energy, 43 (2018) 2197-2206. https://doi.org/10.1016/j.ijhydene.2017.12.082.

[45] D. Wierzbicki, R. Debek, M. Motak, T. Grzybek, M.E. Gálvez, P. Da Costa, Novel Ni-La-hydrotalcite derived catalysts for CO_2 methanation, Catal. Commun. 83 (2016) 5-8. https://doi.org/10.1016/j.catcom.2016.04.021.

[46] N. Bette, J. Thielemann, M. Schreiner, F. Mertens, Methanation of CO_2 over a $(Mg,Al)O_x$ Supported Nickel Catalyst Derived from a (Ni,Mg,Al)-Hydrotalcite-like Precursor, ChemCatChem 8 (2016) 2903 – 2906, https://doi.org/10.1002/cctc.201600469.

[47] D. Wierzbicki, R. Baran, R. Debek, M. Motak, T. Grzybek, M. E. Gálvez, P. Da Costa, The influence of nickel content on the performance of hydrotalcite-derived catalysts in CO_2 methanation reaction, Int. J. Hydrog. Energy 42 (2017) 23548-23555, https://doi.org/10.1016/j.ijhydene.2017.02.148.

[48] W. Gac, Acid–base properties of $Ni–MgO–Al_2O_3$ materials, Appl. Surf. Sci. 257 (2011) 2875-2880. https://doi.org/10.1016/j.apsusc.2010.10.084.

[49] R. Dębek, M. Radlik, M. Motak, M.E. Galvez, W. Turek, P. Da Costa, T. Grzybek, Ni-containing Ce-promoted hydrotalcite derived materials as catalysts for methane reforming with carbon dioxide at low temperature – On the effect of basicity, Catal. Today 257 (2015) 59-65. https://doi.org/10.1016/j.cattod.2015.03.017.

[50] S. Ewald, O. Hinrichsen, On the interaction of CO_2 with Ni-Al catalysts, Appl. Catal. A Gen. 580 (2019) 71-80. https://doi.org/10.1016/j.apcata.2019.04.005.

[51] G. Centi, E.A. Quadrelli, S. Perathoner, Catalysis for CO_2 conversion: a key technology for rapid introduction of renewable energy in the value chain of chemical industries, Energy Environ. Sci. 6 (2013) 1711-1731, https://doi.org/10.1039/C3EE00056G.

[52] C. Janke, M.S. Duyar, M. Hoskins, R. Farrauto, Catalytic and adsorption studies for the hydrogenation of CO_2 to methane, Appl. Catal. B Environ. 152-153 (2014) 184-191, https://doi.org/10.1016/j.apcatb.2014.01.016.

[53] E.A. Morosanu, F. Salomone, R. Pirone, S. Bensaid, Insights on a Methanation Catalyst Aging Process: Aging Characterization and Kinetic Study, Catalysts 10 (2020) 283. https://doi.org/10.3390/catal10030283.

[54] M. Newville, EXAFS analysis using FEFF and FEFFIT, J. Synchrotron Radiat. 8 (2001) 96–100, https://doi.org/10.1107/S0909049500016290.

[55] B. Ravel, M. Newville, ATHENA, ARTEMIS, HEPHAESTUS: data analysis for X-ray absorption spectroscopy using IFEFFIT, J. Synchrotron Radiat 12 (2005) 537–541, https://doi.org/10.1107/S0909049505012719.

[56] C.E. Daza, J. Gallego, J.A. Moreno, F. Mondragón, S. Moreno, R. Molina, CO_2 reforming of methane over Ni/Mg/Al/Ce mixed oxides, Catal. Today 133–135 (2008) 357–366, https://doi.org/10.1016/j.cattod.2007.12.081.

[57] J.M. Fernández, C. Barriga, M.A. Ulibarri, F.M. Labajos, V. Rives, New Hydrotalcite-like Compounds Containing Yttrium, Chem. Mater. 9 (1997) 312-318, https://doi.org/10.1021/cm9603720.

[58] L. Atzori, M.G. Cutrufello, D. Meloni, R. Monaci, C. Cannas, D. Gazzoli, M.F. Sini, P. Deiana, E. Rombi, CO_2 methanation on hard-templated $NiOCeO_2$ mixed oxides, Int. J. Hydrog. Energy 42 (2017) 20689-20702, https://doi.org/10.1016/j.ijhydene.2017.06.198.

[59] W. Wang, Y. Liu, C. Xu, C. Zheng, G. Wang, Synthesis of NiO nanorods by a novel simple precursor thermal decomposition approach, Chem. Phys. Lett. 362 (2002) 119-122, https://doi.org/10.1016/S0009-2614(02)00996-X.

[60] S. Abelló, D. Verboekend, B. Bridier, J. Pérez-Ramírez, Activated takovite catalysts for partial hydrogenation of ethyne, propyne, and propadiene, J. Catal. 259 (2008) 85–95, https://doi.org/10.1016/j.jcat.2008.07.012.

[61] P. Salagre, J.L.G. Fierro, F. Medina, J.E. Sueiras, Characterization of nickel species on several γ-alumina supported nickel samples, J. Mol. Catal. A Chem. 106 (1996) 125-134, https://doi.org/10.1016/1381-1169(95)00256-1.

[62] D. Delgado, B. Solsona, R. Sanchis, E. Rodríguez-Castellón, J.M. López Nieto, Oxidative dehydrogenation of ethane on diluted or promoted nickel oxide catalysts: Influence of the promoter/diluter, Catal. Today (2019), in press, https://doi.org/10.1016/j.cattod.2019.06.063.

[63] J.C. Vedrine, G. Hollinger, D. Tran Minh, Investigations of antigorite and nickel supported catalysts by x-ray photoelectron spectroscopy, J. Phys. Chem. 82 (1978) 1515-1520, https://doi.org/10.1021/j100502a011.

[64] V. Biju, M. Abdul Khadar, Electronic Structure of Nanostructured Nickel Oxide Using Ni 2p XPS Analysis, J. Nanopart. Res. 4 (2002) 247-253, https://doi.org/10.1023/A:1019949805751.

[65] M.A. van Veenendaal, G.A. Sawatzky, Nonlocal screening effects in 2p x-ray photoemission spectroscopy core-level line shapes of transition metal compounds, Phys. Rev. Lett. 70 (1993) 2459-2462, https://doi.org/10.1103/PhysRevLett.70.2459.

[66] J.F. Moulder, W.F. Stickle, P.E. Sobol, K.D. Bomben, J. Chastain (Ed.), Handbook of X-Ray Photoelectron Spectroscopy, Perkin-Elmer Corporation, Eden Prairie, Minnesota, 1992.

[67] V.V. Kaichev, V.I. Bukhtiyarov, M. Hävecker, A. Knop-Gercke, R.W. Mayer, R. Schlögl, The Nature of Electrophilic and Nucleophilic Oxygen Adsorbed on Silver, Kinet. Catal. 44 (2003) 432-440, https://doi.org/10.1023/A:1024459305551.

[68] D. Tichit, F. Medina, B. Coq, R. Dutartre, Activation under oxidizing and reducing atmospheres of Ni-containing layered double hydroxides, Appl. Catal. A Gen. 159 (1997) 241-258. https://doi.org/10.1016/S0926-860X(97)00085-9.

[69] J.I. Di Cosimo, V.K. Díez, M. Xu, E. Iglesia, C.R. Apesteguía, Structure and Surface and Catalytic Properties of Mg-Al Basic Oxides, J. Catal. 178 (1998) 499-510, https://doi.org/10.1006/jcat.1998.2161.

[70] L.J.I. Coleman, W. Epling, R.R. Hudgins, E. Croiset, Ni/Mg–Al mixed oxide catalyst for the steam reforming of ethanol, Appl. Catal. A Gen. 363 (2009) 52-63. https://doi.org/10.1016/j.apcata.2009.04.032.

[71] S. Sato, R. Takahashi, M. Kobune, H. Gotoh, Basic properties of rare earth oxides, Appl. Catal. A Gen. 356 (2009) 57-63, https://doi.org/10.1016/j.apcata.2008.12.019.

[72] Z. Boukha, L. Fitian, M. López-Haro, M. Mora, J.R. Ruiz, C. Jiménez-Sanchidrián, G. Blanco, J.J. Calvino, G.A. Cifredo, S. Trasobares, S. Bernal, Influence of the calcination temperature on the nano-structural properties, surface basicity, and catalytic behavior of alumina-supported lanthana samples, J. Catal. 272 (2010) 121-130, https://doi.org/10.1016/j.jcat.2010.03.005.

[73] P. Marocco, E.A. Morosanu, E. Giglio, D. Ferrero, C. Mebrahtu, A. Lanzini, S. Abate, S. Bensaid, S. Perathoner, M. Santarelli, R. Pirone, G. Centi, CO_2 methanation over Ni/Al hydrotalcite-derived catalyst: Experimental characterization and kinetic study, Fuel 225 (2018) 230-242, https://doi.org/10.1016/j.fuel.2018.03.137.

[74] S. Matthischke, S. Roensch, R. Güttel, Start-up Time and Load Range for the Methanation of Carbon Dioxide in a Fixed-Bed Recycle Reactor, Ind. Eng. Chem. Res. 57 (2018) 6391-6400, https://doi.org/10.1021/acs.iecr.8b00755.

[75] A. Fache, F. Marias, V. Guerré, S. Palmade, Optimization of fixed-bed methanation reactors: Safe and efficient operation under transient and steady-state conditions, Chem. Eng. Sci. 192 (2018) 1124–1137, https://doi.org/10.1016/j.ces.2018.08.044.

[76] M. Biset-Peiró, R. Mey, J. Guilera, T. Andreu, Adiabatic plasma-catalytic reactor configuration: Energy efficiency enhancement by plasma and thermal synergies on CO_2 methanation, Chem. Eng. J. 393 (2020) 124786. https://doi.org/10.1016/j.cej.2020.124786.

[77] Y. Yan, Y. Dai, H. He, Y. Yu, Y. Yang, A novel W-doped Ni-Mg mixed oxide catalyst for CO_2 methanation, Appl. Catal. B Environ. 196 (2016) 108–116, https://doi.org/10.1016/j.apcatb.2016.05.016.

[78] A. Bengaouer, J. Ducamp, I. Champon, R. Try, Performance evaluation of fixed-bed, millistructured, and metallic foam reactor channels for CO_2 methanation, Canadian J. Chem. Eng. 96 (2018) 1937-1945, https://doi.org/10.1002/cjce.23140.

[79] B. Mutz, H.W.P. Carvalho, S. Mangold, W. Kleist, J.-D. Grunwaldt, Methanation of CO_2: Structural response of a Ni-based catalyst under fluctuating reaction conditions unraveled by operando spectroscopy, J. Catal. 327 (2015) 48–53, https://doi.org/10.1016/j.jcat.2015.04.006.

[80] L.R. Winter, R. Chen, X. Chen, K. Chang, Z. Liu, S.D. Senanayake, A.M. Ebrahim, J.G. Chen, Elucidating the roles of metallic Ni and oxygen vacancies in CO_2 hydrogenation over Ni/CeO_2 using isotope exchange and in situ measurements, Appl. Catal. B Environ. 245 (2019) 360-366, https://doi.org/10.1016/j.apcatb.2018.12.069.

[81] C.A. Gandhi, Y.S. Wu, Strong, Deep-Level-Emission Photoluminescence in NiO Nanoparticles, Nanomaterials 7 (2017), https://doi.org/10.3390/nano7080231.

Support Information

Unravelling the role of metallic and basic sites in coprecipitated Ni catalysts promoted with rare-earth elements for CO₂ methanation

Phuoc Hoang Ho[1], Giancosimo Sanghez de Luna[1], Saverio Angelucci[1,2], Andrea Canciani[1,2], Wilm Jones[2,3], Donato Decarolis[2], Francesca Ospitali[1], Elena Rodriguez Aguado[4], Enrique Rodríguez-Castellón[4], Giuseppe Fornasari[1], Angelo Vaccari[1], Andrew M. Beale[2,3]*, Patricia Benito[1,]*

[1] Dip. Chimica Industriale "Toso Montanari", Università di Bologna, Viale Risorgimento 4, 40136, Bologna, Italy

[2] Research Complex at Harwell, Rutherford Appleton Laboratories, Harwell, OX11 0FA, Oxon. UK

[3] Department of Chemistry, 20 Gordon Street, University College London, WC1H 0AJ, London. UK

[4] Departamento de Química Inorgánica, Facultad de Ciencias, Universidad de Málaga, 29071 Málaga, Spain

* patricia.benito3@unibo.it

* andrew.beale@ucl.ac.uk

Figure S1. XRD patterns of NiAl and NiXAl hydrotalcite-like precursors (a); calcined and used NiYAl and NiCeAl catalysts (b). The reference patterns are from the International Centre Diffraction Data (ICDD), PDF4-2020.
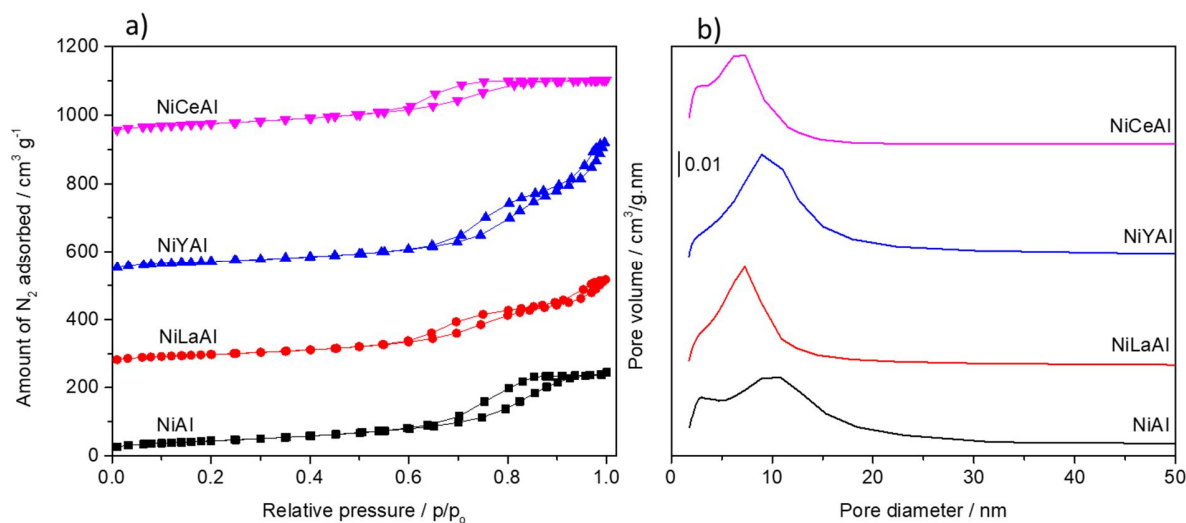
Figure S2. Isotherms of nitrogen adsorption/desorption (a) and BJH pore size distribution (b) of NiAl and NiXAl catalysts.

N_2 adsorption/desorption of the catalysts are type IV isotherms according to the classification of IUPAC (Figure S2a) [S1]. The differences in the adsorption/desorption steps are related to pore size dimensions. BJH curves (Figure S2b) confirm that smaller pores are present in the Ce-containing sample (two main peaks around 3 and 7 nm) in comparison to the Ni/Al sample (main distribution at around 3 and 10 nm). NiLaAl and NiYAl catalysts have a more complex isotherm shape (Figure S2a). The first part of the isotherms for La- and Y-containing samples are rather similar to those of Ce- and Ni/Al catalysts, respectively, but the plateau at high relative pressures is absent and a continuous N_2 uptake occurs for both of them.
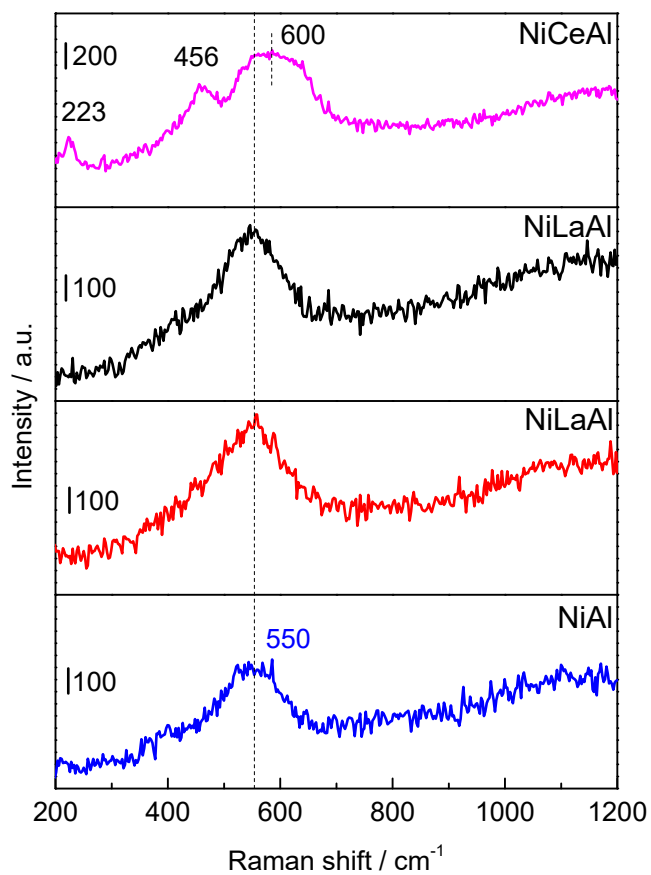
Figure S3. Raman spectra of NiAl and NiXAl catalysts.

In the Ce-containing sample, besides the typical F_{2g} mode of cubic fluorite CeO_2 at 461 cm^{-1}, the shoulder at *ca.* 600 cm^{-1} and the small peak at 223 cm^{-1} suggest the presence of lattice defects, such as those in a Ni-CeO_2 solid solution, introduced into the structure to maintain the neutrality [S2].
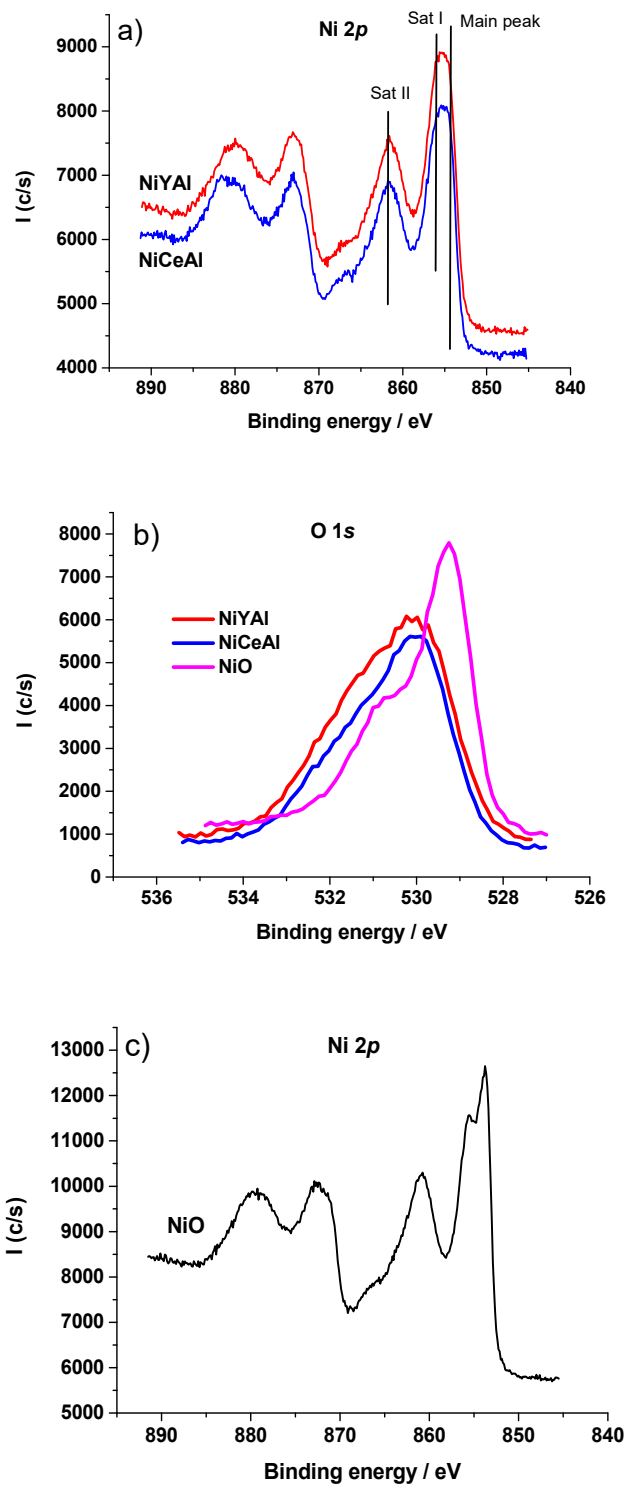
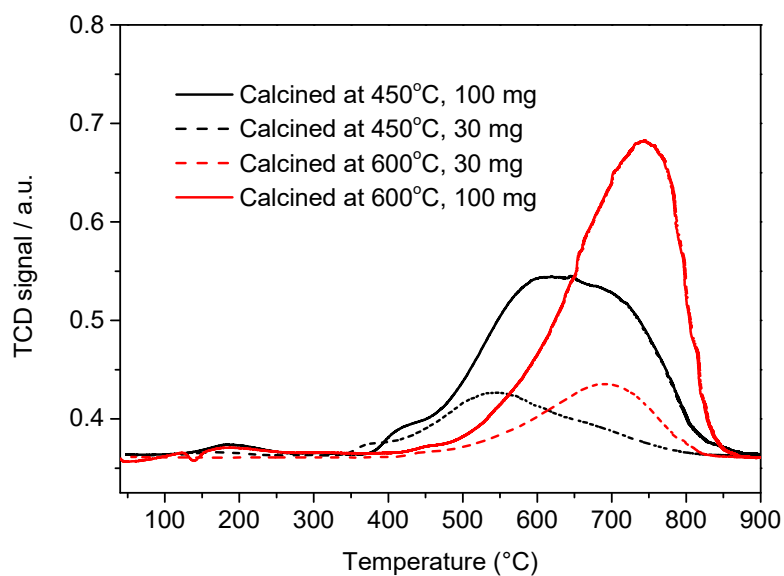**Figure S4.** XPS of NiYAl and NiCeAl catalysts: a) Ni $2p_{3/2}$, b) O $1s$ and of NiO as a reference Ni $2p$ c).
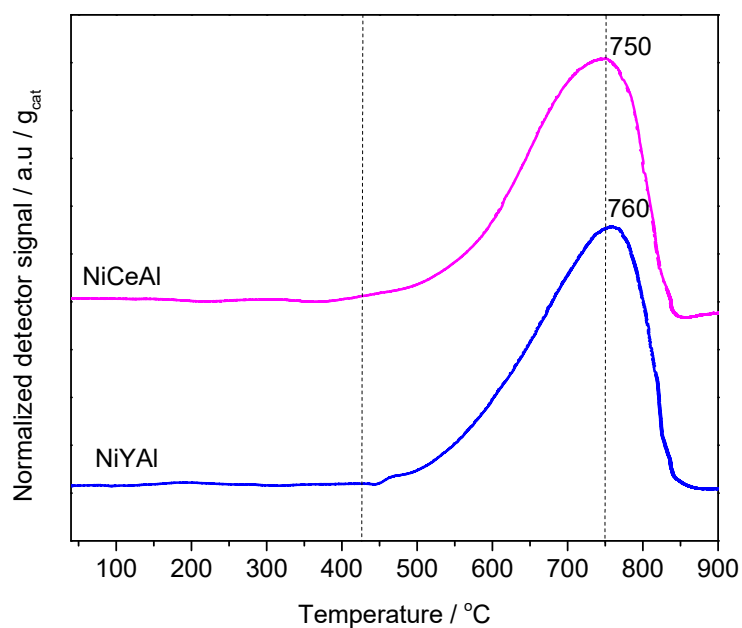
Figure S5. H_2-TPR profiles of NiYAl and NiCeAl catalysts.

Table S1. Hydrogen consumption and reducible degree of NiAl and NiXAl catalysts

| Sample	H_2 consumption / mmol g^{-1}	H_2 consumption / mmol g_{Ni}^{-1}	Reducible degree / %
NiAl	9.4	14.6	86
NiLaAl	7.5	13.4	79
NiYAl	7.5	12.9	76
NiCeAl	7.4	13.2	78

It is well-known that the reduction temperature of HT-derived catalysts increases with the calcination temperature of the precursors [S3-S5]. This is also confirmed here by comparing the H$_2$-TPR profiles of the NiLaAl sample calcined at 600 °C and 450 °C, the latter widely used in the literature to obtain methanation catalysts [S6-S8] (Fig. S6). However, the XRD patterns of these catalysts (Fig. S7a) show that at 600 °C the hardly reducible NiAl$_2$O$_4$ spinel phase does not crystallize [S3].


Figure S6. Effect of calcination temperature and mass of samples on H$_2$-TPR profiles of NiLaAl catalyst.
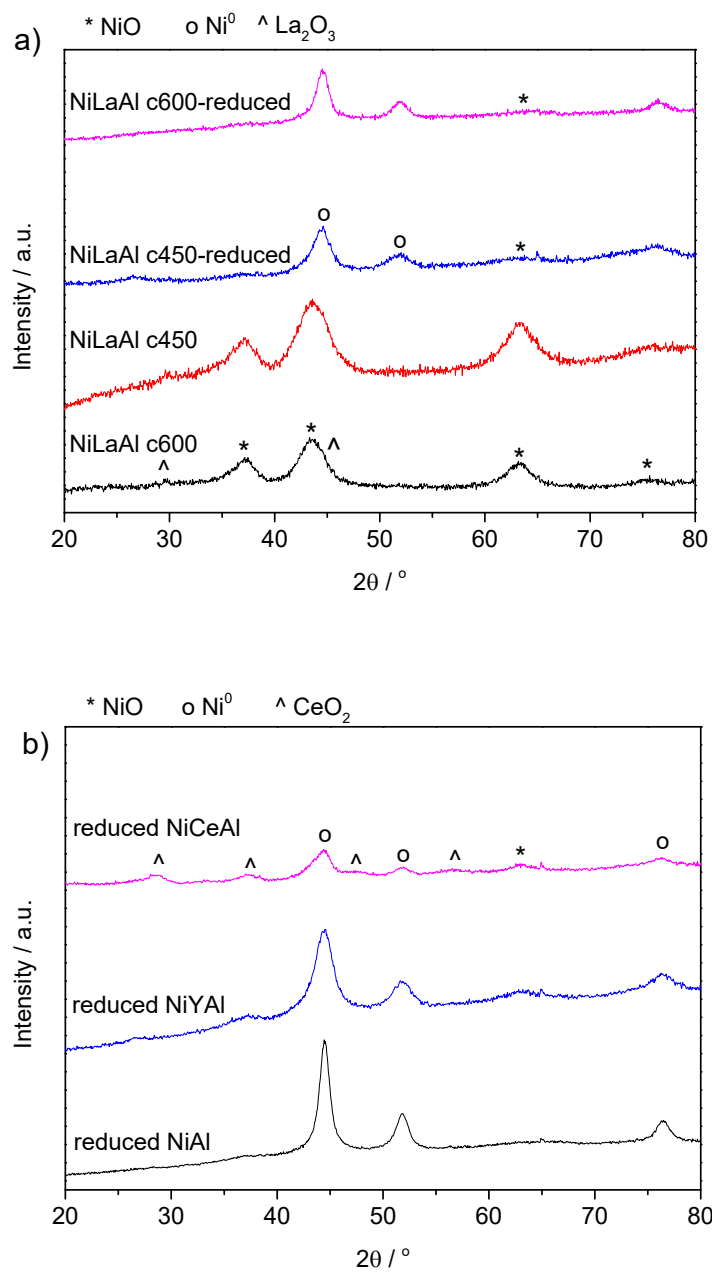
Figure S7. XRD patterns of: a) NiLaAl catalysts calcined at 450 °C (c450) and 600°C (c600) before and after reduction; b) NiAl, NiYAl and NiCeAl catalysts after reduction.
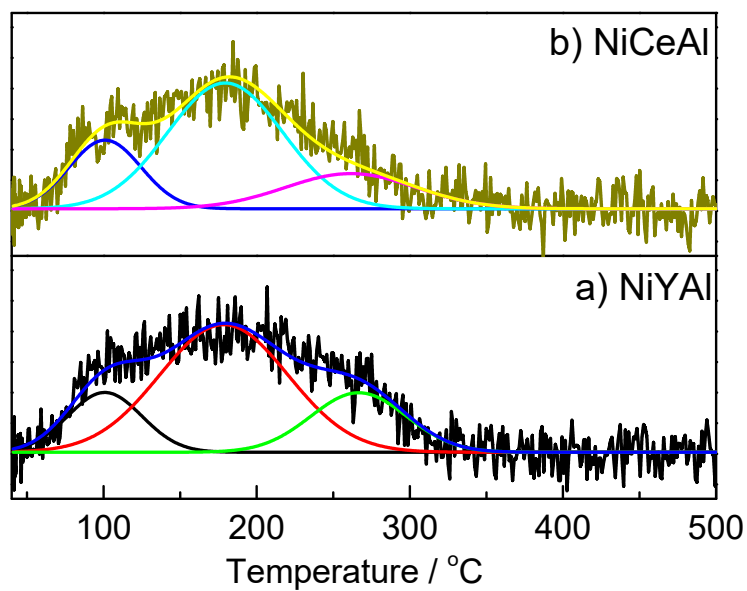
Figure S8. CO_2-TPD profiles of NiYAl and NiCeAl catalysts. Detailed information of the deconvoluted peaks are summarized in Table 3.
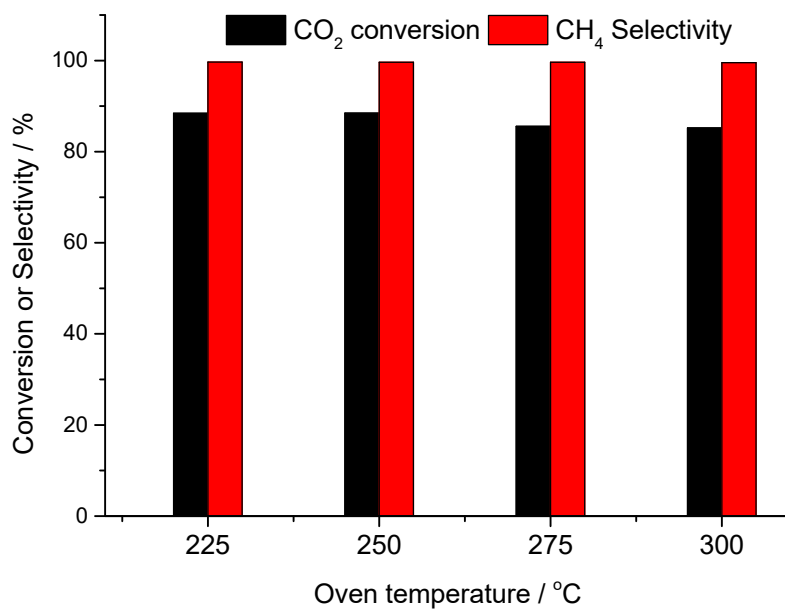
Figure S9. CO_2 conversion and CH_4 selectivity on 120 mg of NiLaAl catalyst (diluted with quarz). Reaction conditions: Total flow rate 240 ml min^{-1}; $CO_2/H_2/N_2$ = 1/4/1 v/v; 120 L g^{-1} h^{-1}.
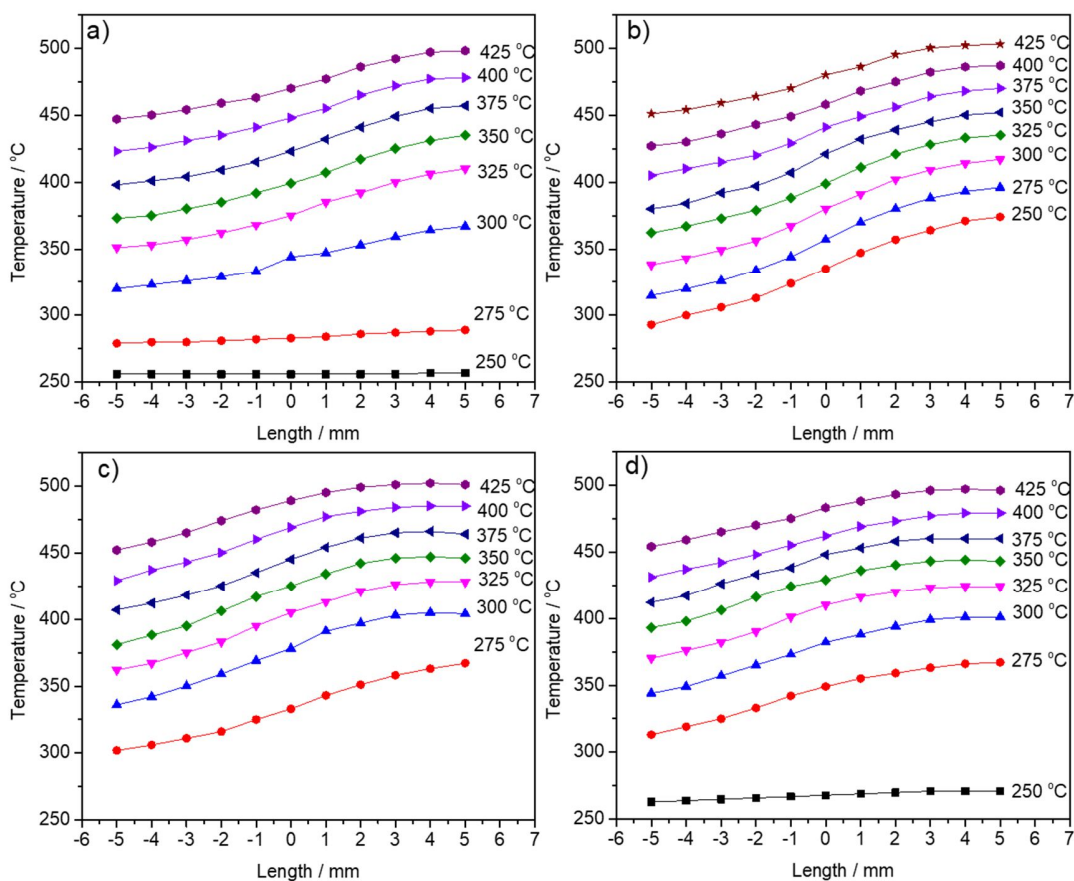
**Figure S10.** Temperature profiles of NiXAl catalyst during the CO_2 methanation: a) NiAl, b) NiLaAl, c) NiYAl, and d) NiCeAl. Total flow rate 240 ml min^{-1}, $CO_2/H_2/N_2$ = 1/4/1 v/v, 30 mg catalyst diluted in 470 mg quartz, 480 L g^{-1} h^{-1}. Note that the catalytic bed starts at position x = 0 and the values on the y-axis are oven temperatures.
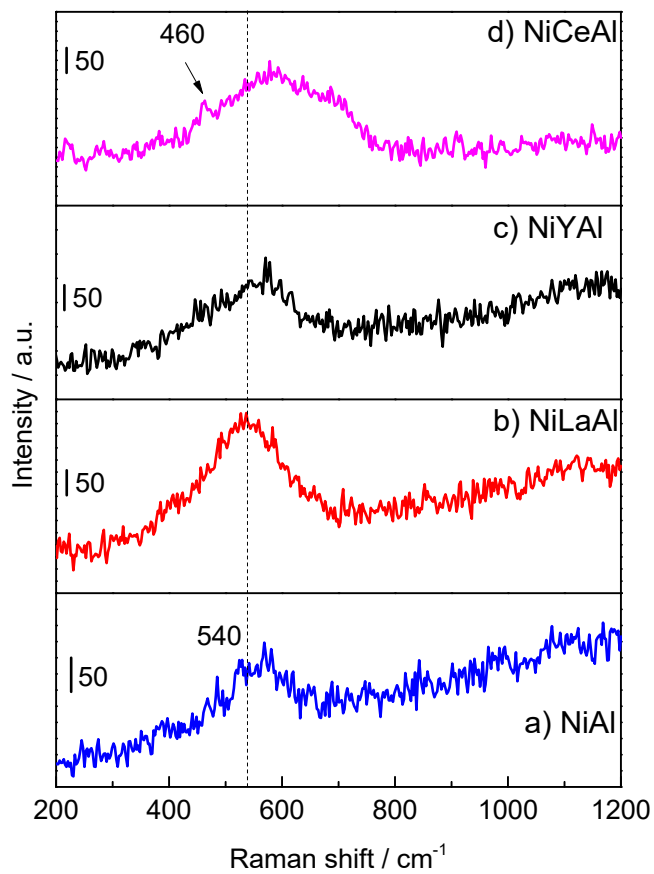
Figure S11. Raman spectra of NiAl and NiXAl used catalysts.
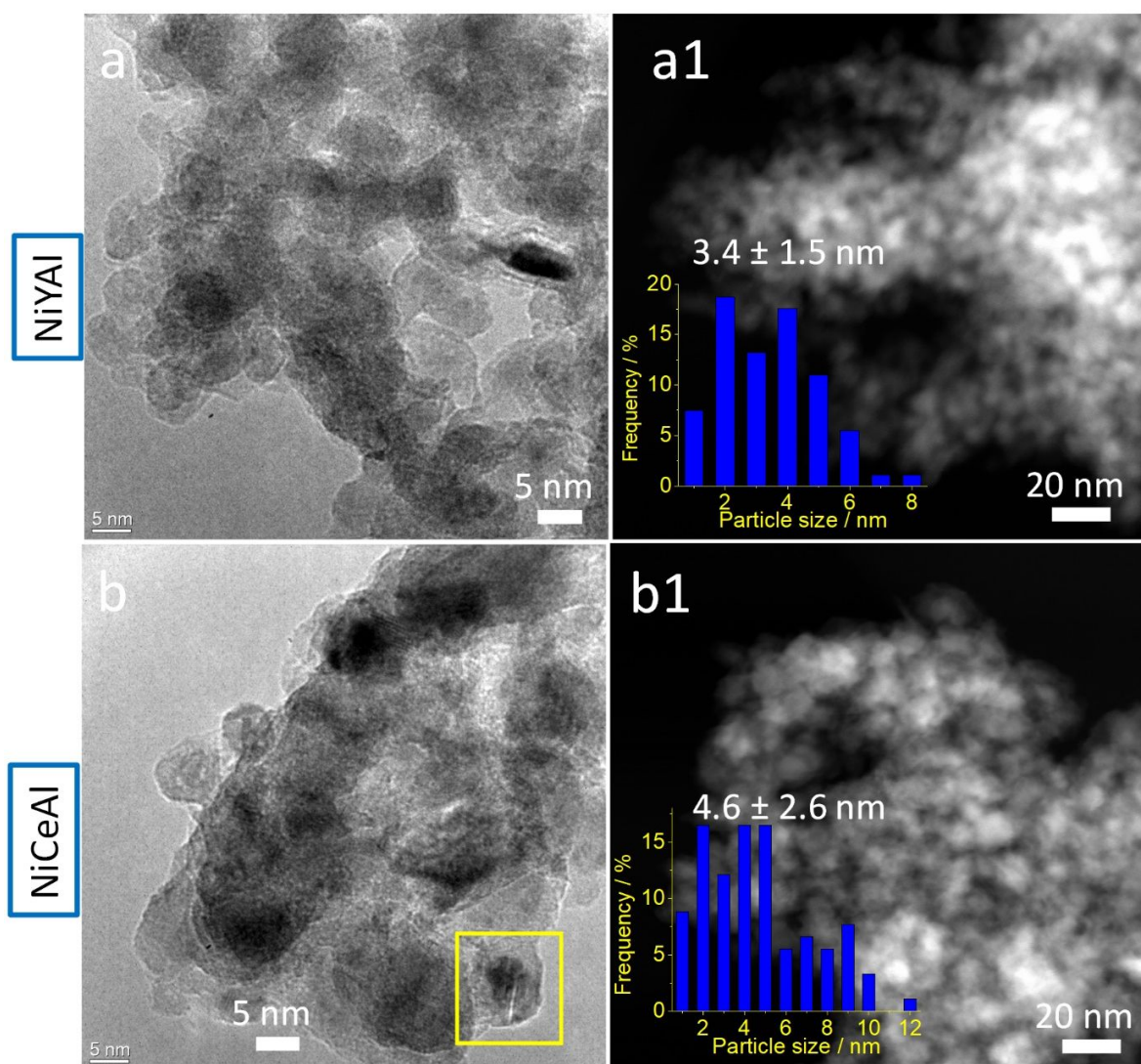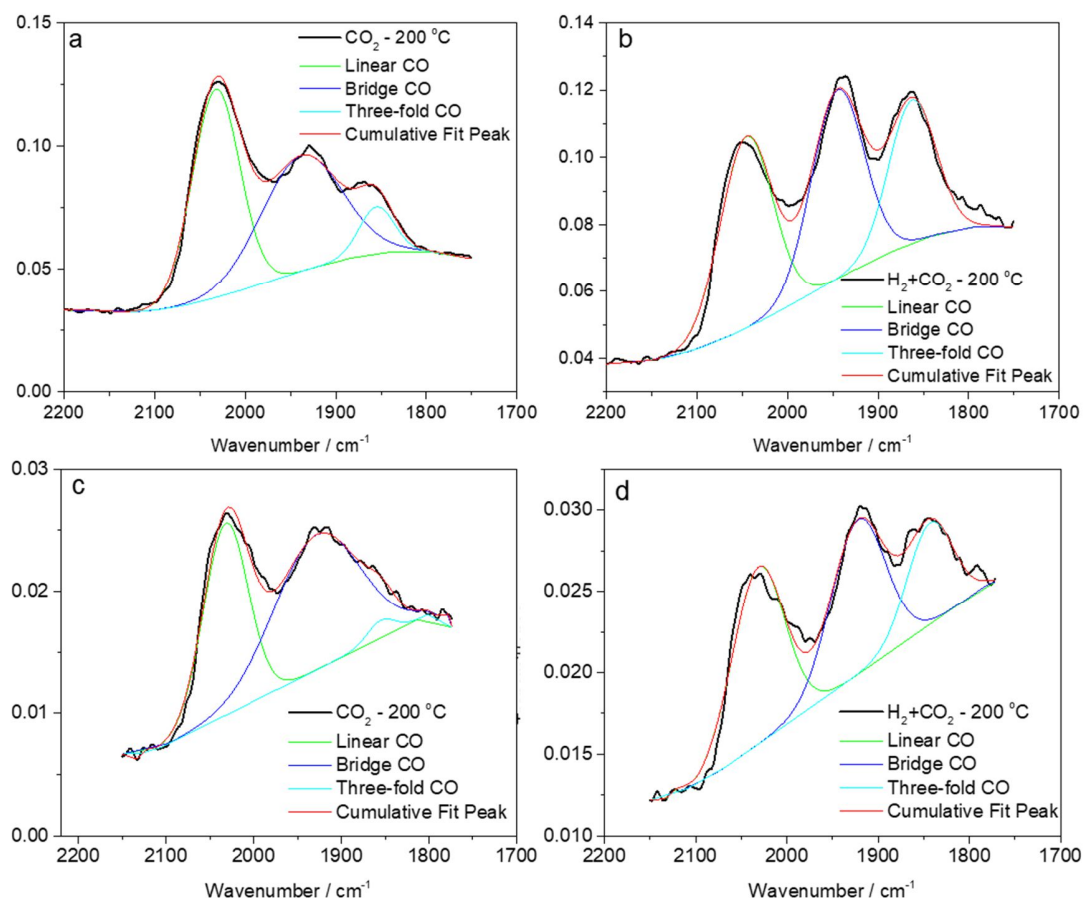
Figure S12. HRTEM images (a, b) and STEM images (a1, b1) and Ni particle size distribution (insets of Fig. a1, b1) of NiYAl and NiCeAl used catalysts: a, a1) NiYAl; b, b1) NiCeAl.
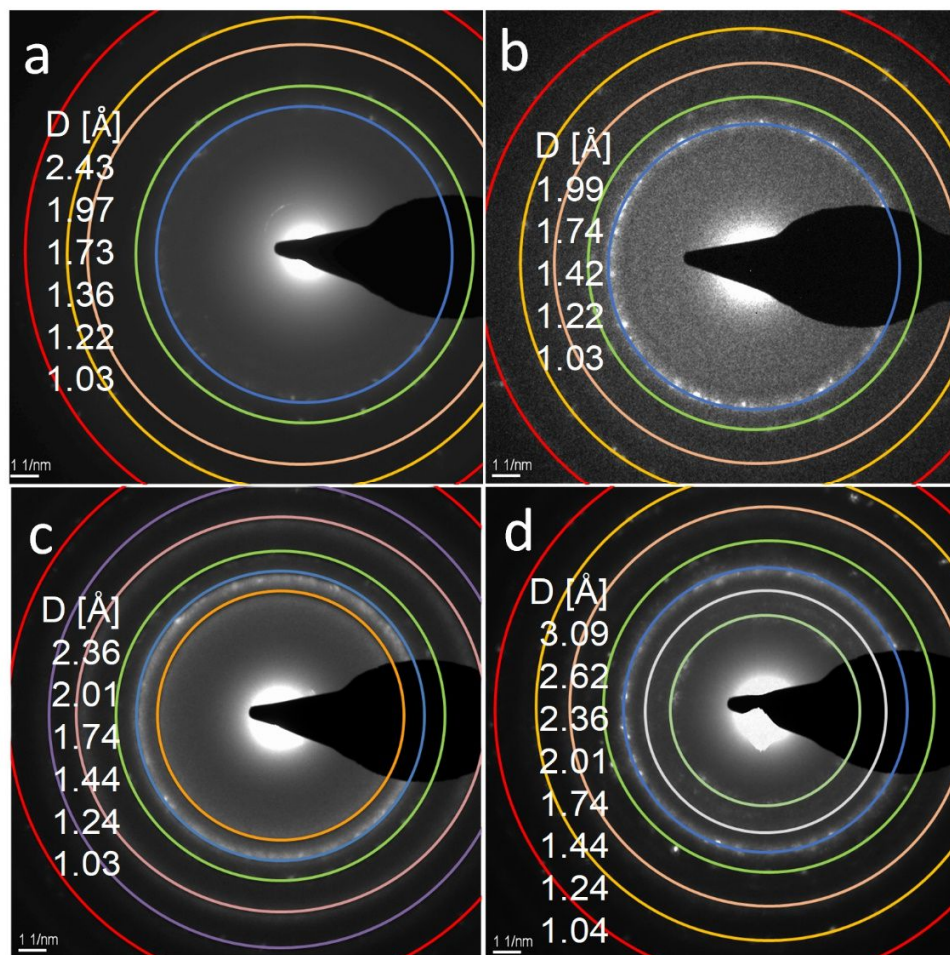
Figure S13. Fast Fourier Transformation of SAED from HR-TEM analyses of NiAl and NiXAl used catalysts: a) NiAl, b) NiLaAl, c) NiYAl, and d) NiCeAl.

Figure S14. Distribution of different types of CO adsorbed on Ni particles of NiAl (a, b) and NiLaAl catalysts (c,d) from DRIFTS measurements (absorbance mode). Note that a) and c in CO_2 at 200 °C; b) and d in mixture of $H_2/CO_2 = 4/1$ v/v. Percentages of peak areas deconvoluted by Origin software are presented in following Table:

Sample	200 °C	Linear	Bridge	Three-fold
NiAl	Adsorb	48	45	8
	React	38	37	25
NiLaAl	Adsorb	41	56	2
	React	41	38	21

Table S2. Comparison of CH_4 productivity of the catalysts in this work and recent publications in literature

Catalyst	Ni / wt%	Total flow /mL min^{-1}	CO_2 vol.%	GHSV / h^{-1}	WHSV / L g^{-1} h^{-1}	Pressure / bar	Temp. / °C	CH_4 Productivity / L g$_{Ni}$$^{-1}$ h^{-1}	Ref.
NiLaAl	56	240	0.17	38200	480	atmospheric	325	101.2	
NiYAl	58	240	0.17	38200	480	atmospheric	325	83.9	This
NiCeAl	56	240	0.17	38200	480	atmospheric	325	94.6	work
NiAl	64	240	0.17	38200	480	atmospheric	325	67.4	
Ni/La$_2$O$_3$	9.3	200	0.16	12000	30	atmospheric	350	17.3	
Ni/CeO$_2$	10.6	200	0.16	12000	30	atmospheric	350	34.9	[S9]
Ni/PrO$_x$	10.7	200	0.16	12000	30	atmospheric	350	29.7	
Ni/CaO-Al$_2$O$_3$	23	40	0.12	15000	48	atmospheric	400	20.1	[S10]
Ni/Fe-Al$_2$O$_3$	25	500	0.2	10000	200	5	300	142.6	[S6]
Ni-La/Al$_2$O$_3$	13.6	80	0.06	55000	54	atmospheric	350	21.6	[S11]
NiWMgO$_x$	16.9	100	0.05	40000	60	atmospheric	300	14.4	[S12]
NiMnAlO$_x$	36.3	225	0.1	200000	150	8	350	132.5	[S7]
NiFeAlO$_x$	39.6	225	0.1	200000	150	8	350	121.5	[S7]
Ni$_3$Fe/Al$_2$O$_3$	12.9	108	0.1	4811	6	6	358	11.7	[S13]
Ni/Y$_2$O$_3$	10	100	0.05	40000	60	atmospheric	350	26.1	[S14]

Table S3. Improvement in the chemical-physical properties and CO_2 methanation activity of HT-derived NiAl catalysts by the presence rare earth metals

Technique	Catalyst property	NiLaAl	NiYAl	NiCeAl
XRD	NiO crystallite size	✓✓✓	✓✓✓	—
HR-TEM	Ni^0 particle size	✓✓✓	✓✓✓	—
H$_2$-TPR	Reducibility	—	—	—
CO$_2$-TPD	Basicity	✓✓✓	✓✓	✓
DRIFTs	Associative CO_2 mechanism	✓✓✓	n.d.	n.d
XPS	Surface Ni/Al ratio	✓✓✓	—	✓✓
XAFS	Stabilization of metallic Ni	✓✓	n.d.	n.d.
Methanation tests	Catalytic activity	✓✓✓	✓✓	✓

— not different; number of ticks (✓) indicates level of improvement, n.d. not determined

References

[S1] M. Thommes, K. Kaneko, A. V. Neimark, J. P. Olivier, F. Rodriguez-Reinoso, J. Rouquerol and K. S. W. Sing, Pure Appl. Chem. 2015, 87, 1051–1069.

[S2] L. Atzori, M.G. Cutrufello, D. Meloni, R. Monaci, C. Cannas, D. Gazzoli, M.F. Sini, P. Deiana, E. Rombi, Int. J. Hydrog. Energy 42 (2017) 20689-20702.

[S3] O. Clause, M. Goncalves Coelho, M. Gazzano, D. Matteuzzi, F. Trifirò, A. Vaccari, Applied Clay Science 8 (1993) 169-186

[S4] I. Pettiti, D. Gazzoli, P. Benito, G. Fornasari, A. Vaccari, RSC Adv. 5 (2015) 82282-82291.

[S5] S. Abelló, D. Verboekend, B. Bridier, J. Pérez-Ramírez, J. Catal. 259 (2008) 85–95

[S6] C. Mebrahtu, S. Abate, S. Chen, A.F. Sierra Salazar, S. Perathoner, F. Krebs, R. Palkovits, G. Centi, Energy Technol. 6 (2018) 1196–1207.

[S7] T. Burger, F. Koschany, O. Thomys, K. Köhler, O. Hinrichsen, Appl. Catal. A Gen. 558 (2018) 44–54.

[S8] D. Beierlein, D. Häussermann, M. Pfeifer, T. Schwarz, K. Stöwe, Y. Traa, E. Klemm, Appl. Catal. B Environ. 247 (2019) 200–219.

[S9] V. Alcalde-Santiago, A. Davó-Quiñonero, D. Lozano-Castelló, A. Quindimil, U.I De-La-Torre, B. Pereda-Ayo, J.A. González-Marcos, J.R. González-Velasco, A. Bueno-López, ChemCatChem 11 *(*2019) 810–819.

[S10] A. Fache, F. Marias, V. Guerré, S. Palmade, Chem. Eng. Sci. 192 (2018) 1124–1137.

[S11] G. Garbarino, C. Wang, T. Cavattoni, E. Finocchio, P. Riani, M. Flytzani-Stephanopoulos, G. Busca, Appl. Catal. B Environ. 248 (2019) 286-297.

[S12] S. Ratchahat, M. Sudoh, Y. Suzuki, W. Kawasaki, R. Watanabe, C. Fukuhara, J. CO_2 Utiliz. 24 (2018) 210-219.

[S13] B. Mutz, M. Belimov, W. Wang, P. Sprenger, M.A. Serrer, D. Wang, P. Pfeifer, W. Kleist, J.D. Grunwaldt, ACS Catal. 7 (2017) 6802–6814.

[S14] H. Muroyama, Y. Tsuda, T. Asakoshi, H. Masitah, T. Okanishi, T. Matsui, K. Eguchi, J. Catal. 343 (2016) 178–184.